Ocean Engineering 328 (2025) 121007

Contents lists available at ScienceDirect

Ocean Engineering

journal homepage: www.elsevier.com/locate/oceaneng

Research paper

Integrated CFD and hydrodynamic correction approach for load response analysis of floating offshore wind turbine

Ho-Seong Yang [a], Ali Alkhabbaz [b], Young-Ho Lee [a,*]

[a] Center for Offshore Wind & Green Hydrogen Ammonia Research, Korea Maritime and Ocean University, Busan, Republic of Korea
[b] Sustainable Energy Engineering Department, College of Engineering, University of Mosul, Mosul, 41002, Iraq

ARTICLE INFO

Keywords:
Hydrodynamic correction
Load response analysis
Offshore energy
Floating wind turbine
CFD

ABSTRACT

This study investigates the load response of a 10 MW FOWT mounted on a semi-submersible platform using CFD and hydrodynamic correction methods. The primary objective is to derive generalized correction coefficients through free decay simulations and evaluate the load response under regular wave conditions. To achieve this, three correction approaches, damping coefficient-based, drag coefficient-based, and a hybrid combining both were compared. A newly designed 10 MW semi-submersible substructure connected by pontoons was employed instead of the extensively studied OC4 DeepCwind model. The analysis revealed that the correction method relying solely on damping coefficients failed to capture critical load responses under regular wave conditions and demonstrated inaccuracies. In contrast, the hybrid correction method, which incorporates both drag and damping coefficients, better captured viscous effects and improved damping accuracy, leading to more accurate load response predictions for the 10 MW semi-submersible FOWT. These findings highlight the necessity of considering both free decay results and real-world environmental conditions when determining correction coefficients to enhance prediction accuracy. This study evaluates various correction approaches to enhance hydrodynamic modeling accuracy of FOWTs.

1. Introduction

To combat climate change, the transition to alternative energy sources is becoming increasingly urgent, as traditional fossil fuels remain the dominant energy providers (Eurostat, 2019; Edirisinghe et al., 2023). Among renewable options, wind energy has experienced significant growth over recent decades and now ranks as the second-largest source of power generation, surpassed only by hydropower. Offshore regions hold the majority of high-quality wind resources, offering immense potential for energy development. According to Musial et al. the global offshore wind energy sector is projected to achieve a capacity of 380 GW–394 GW by 2032, representing a nearly sixfold increase within the next decade (Musial et al., 2023). Notably, about 70 % of these offshore wind resources are located at depths exceeding 60 m. To harness this potential economically, floating substructures are expected to play a critical role. Depending on site-specific conditions, a variety of floating platforms, including tension leg platforms (TLPs), spar platforms, and semi-submersible platforms are being considered for FOWT. Currently, semi-submersible platforms are the preferred choice, with 80 % of active floating offshore wind projects opting for this design. For such structures, accurate prediction of wave-induced structural loads is essential, as these forces are more complex than those experienced by fixed installations (Yang et al., 2023, 2024a; Daabo et al., 2024).

Extensive research has been undertaken to enhance the accuracy of load response predictions for floating structures. In the OC5 project, Robertson et al. conducted a comparative study analyzing simulation results for a floating wind semi-submersible structure against experimental data obtained from a scaled test campaign at the Maritime Research Institute Netherlands (Robertson et al., 2017). Their findings demonstrated that medium-fidelity analysis tools effectively captured dynamic interactions in the wave-frequency domain. However, consistent underpredictions were noted in the low-frequency domain. These low-frequency excitations were attributed to the nonlinear interaction of wave components. The study concluded that the combined effects of underestimating nonlinear loads and overestimating system damping resulted in the underestimation of motion responses. Notably, most advancements in predicting load responses for such semi-submersible structures have focused on the DeepCwind floater (Wang et al., 2022a; Robertson et al., 2014a, 2018, 2019, 2020; Wendt et al., 2016).

Numerous studies have employed CFD techniques to advance

* Corresponding author.
E-mail address: lyh@kmou.ac.kr (Y.-H. Lee).

https://doi.org/10.1016/j.oceaneng.2025.121007
Received 16 December 2024; Received in revised form 4 March 2025; Accepted 15 March 2025

Abbreviation

CFD	Computational Fluid Dynamic
DoF	Degrees of Freedom
FOWT	Floating Offshore Wind Turbine
FVM	Finite Volume Method
PBDC	Potential-Based Dynamic Code
RAO	Response Amplitude Operator
RANS	Reynolds Averaged Navier Stokes
VoF	Volume of Fluid

understanding in marine and offshore wind energy systems. Zhou et al. (2021) investigated the application of focused wave dynamics to FOWT systems using CFD simulations. In marine research, the effects of wave patterns focused waves, irregular waves, and reconstructed focused waves were analyzed using the NREL 5 MW semi-submersible FOWT model. Additionally, Alkhabbaz et al. (2024) conducted high-fidelity CFD simulations to explore the impact of semi-submersible platform surge responses on the aerodynamic performance of a 5-MW wind turbine under extreme environmental conditions.

The dynamic motion response, mooring line tension, turbine thrust, and power output of FOWTs were investigated in several studies utilizing CFD and experimental approaches. Wang et al. explored CFD-based predictions of a FOWT under low-frequency wave excitation, addressing the underestimation of nonlinear low-frequency responses in semi-submersible platforms by mid-fidelity engineering tools. Their findings demonstrated strong agreement between CFD simulations and experimental data, validating the method (Wang et al., 2021). Clement et al. assessed the Morison approach for hydrodynamic modeling of a cylinder intersecting the free surface. By deriving Morison coefficients for individual slices of the cylinder, they accurately predicted total loads on the structure, although discrepancies were noted near the free surface, highlighting limitations of the Morison equation in these regions (Clément et al., 2022). In another study, Wang et al. examined the hydrodynamic response of the DeepCwind semi-submersible platform under regular waves using CFD. They evaluated metrics such as surge, heave, pitch RAO, mean surge offset, and zero-frequency surge QTF, finding close alignment with experimental results within verification uncertainties. However, deviations in the mean surge offset and zero-frequency surge QTF were attributed to differences in mooring models and the effects of suspended cable bundles, which were not included in simulations (Wang et al., 2022b). Zou et al. analyzed the short-term hydrodynamic response of the Three Gorges Leading semi-submersible platform using both AQWA and CFD models. Their comparative analysis revealed that while displacement time-history curves from the two codes were similar, notable differences were observed in surge, roll, and pitch directions, highlighting limitations of the AQWA tool under specific conditions (Zou et al., 2023). Similarly, Zhang et al. combined CFD and high-order spectral (HOS) methods to enhance the accuracy of low-frequency response predictions for the DeepCwind platform, outperforming traditional tools such as OpenFAST (Zhang et al., 2023). Yang et al. compared environmental load factors on a semi-submersible FOWT under extreme conditions using CFD and potential-based codes. This study quantified prediction errors and provided insights into the contributions of various environmental load factors to system responses under extreme conditions (Yang et al., 2024b). These investigations collectively highlight the strengths and limitations of CFD and engineering tools in predicting FOWT performance and provide critical insights for improving hydrodynamic modeling and response prediction accuracy.

Hydrodynamic forces are typically estimated using a hybrid approach that integrates additional viscous forces into the potential flow model through diffraction and radiation terms, supplemented by Morison's equation. Accurate selection of viscous drag coefficients is essential to account for fluid resistance and secondary damping effects. In floating offshore wind energy engineering, calibrating these drag coefficients against experimental data is critical. Decay tests are a widely adopted method for determining these coefficients due to their practicality (Wendt et al., 2017). Recent research has demonstrated that assigning case-specific drag coefficients can significantly enhance the agreement between simulated and experimental low-frequency platform responses (Petter et al., 2016; Kvittem et al., 2018; Lemmer (nSandner) et al., 2018). Pegalajar-Jurado et al. identified the damping characteristics of the TetraSpar floater using Operational Modal Analysis (OMA) and found that damping coefficients vary significantly with wave height and motion amplitude (Pegalajar-Jurado et al., 2025–02). Their study suggested that using only free decay tests for damping calibration may not fully capture complex hydrodynamic interactions in operational conditions. Similarly, Böhm et al. developed an optimization-based calibration method for hydrodynamic drag coefficients in semi-submersible platforms, comparing it with traditional free decay test-based calibration (Böhm et al., 2020). Their approach incorporated experimental data from irregular wave conditions to optimize drag coefficients, improving the accuracy of hydrodynamic response predictions. However, while manual parameter fitting and calibration coefficient identification through additional environmental load condition analysis and experiments can improve the accuracy of potential flow analysis tools, they may be inefficient during the early design phase. Free decay tests remain a reliable fundamental method for initial damping coefficient identification, providing essential baseline data before incorporating more complex sea states. Therefore, although they may not be optimal for all conditions, establishing globally applicable calibration coefficients using free decay data can contribute to improving efficiency in the early stages of research and development.

This study aims to identify optimal calibration coefficients during the primary calibration phase using decay motion data, before selecting appropriate resistance coefficients for various load cases through detailed analysis. Additionally, it investigates the motion characteristics influenced by these calibration coefficients. Three calibration methodologies were employed: (1) calibration based solely on the damping coefficient, (2) calibration using only the drag coefficient, and (3) a hybrid approach integrating both drag and damping coefficients. Instead of the widely studied OC4 DeepCwind model, this research utilized a novel 10 MW semi-submersible substructure connected by pontoons. Calibration was conducted using free decay motion results, and the calibrated engineering model was evaluated in a fully coupled configuration under regular wave conditions representative of operational scenarios.

2. Analysis method and model description

This study introduces a novel method for selecting an appropriate correction coefficient to enhance the accuracy of CFD within a potential-based dynamic simulation framework. To achieve this, CFD free decay simulations were conducted, and their results were systematically compared with those of the PBDC. This comparison facilitated the derivation of the correction coefficient essential for fully coupled simulations. The PBDC employs time-domain analysis to evaluate the load response over time in fully coupled scenarios. This time-domain analysis is inherently nonlinear, with mass, damping, stiffness, and load parameters recalculated at each time step based on instantaneous and time-varying conditions, as described by equation (1).

$$\mathrm{M}\ddot{x}(t) + C\dot{x}(t) + Kx(t) = F_{external}(t) \tag{1}$$

Here, $\mathrm{M}\ddot{x}(t)$ represents the inertial force due to the mass matrix M, which is proportional to the acceleration of the structure, and $C\dot{x}(t)$ represents the damping force due to the damping matrix C, which is proportional to the velocity of the structure. $Kx(t)$ represents the restoring force due to

the stiffness matrix K, which reflects the structure's tendency to return to its original position. The added mass, stiffness, and damping required to compute the equation of motion for these components are calculated through potential theory-based hydrodynamic analysis. Additionally, the load RAO values calculated in the frequency domain through hydrodynamic analysis are utilized in time-domain simulations for specific wave frequencies. $F_{external}(t)$ includes external forces such as wave forces, tidal forces, tension, aerodynamic forces, gravity, buoyancy, and other external forces.

The hydrodynamic data derived using potential flow theory is based on the assumption of an inviscid fluid, which inherently minimizes the representation of viscous damping effects. When these effects are not explicitly accounted for, the predicted responses may deviate significantly from actual physical behavior. To address this limitation, two primary approaches are commonly employed to incorporate damping effects into potential flow-based dynamic models. The first approach involves the direct application of a damping coefficient, while the second introduces a Morison element to account for drag-induced damping. This study evaluates three correction techniques: the two aforementioned methods and a hybrid approach that integrates both.

The damping coefficient utilized in the initial method was established based on the damping ratio obtained from CFD free decay simulations. When applying the damping coefficient, the time-domain analysis distinguishes between linear and quadratic damping, as outlined in Equation (2).

$$M\ddot{x}(t) + C_{linear}\dot{x}(t) + C_{quadratic}|\dot{x}(t)|\dot{x}(t) + Kx(t) = F_{external}(t) \tag{2}$$

Here, C_{linear} refers to the linear damping coefficient, and $C_{quadratic}$ refers to the quadratic damping coefficient.

In the second method, the drag coefficient values corresponding to the geometry proposed in previous studies were used in conjunction with the Morison equation. The Morison equation is used to calculate the external hydrodynamic forces acting on a structure. Forces exerted on the structure due to fluid motion such as waves and currents are treated as external forces. The external force in the Morison equation is divided into inertial force and drag force, representing forces arising from external environmental conditions acting on the structure. The Morison equation is expressed as equation (3):

$$F_{morison}(t) = C_m \rho V \frac{dU(t)}{dt} + \frac{1}{2} C_d \rho A |U(t)| U(t) \tag{3}$$

This external force corresponds to $F_{external}(t)$ in the equation of motion, and in the PBDC, the interaction between the fluid and structure is calculated at each time step, and this external force is reflected in the simulation. When implementing the damping effect using the Morison element, as in the second method, the drag coefficient values are not derived from geometries that perfectly match the components used in this study's floater. Therefore, there may be discrepancies in comparison with free decay results. To improve this, an additional damping coefficient was applied in the hybrid method.

The hybrid method considers both C_{linear}, $C_{quadratic}$, and $F_{morison}(t)$ used in equations (2) and (3). Since the Morison element already reflects some degree of the damping effect, the damping ratio derived from the free decay results cannot be used directly. Therefore, the damping coefficients for each DoF were adjusted to derive optimal values that make the motion response of the PBDC match as closely as possible to the CFD free decay results. The specific process for determining the damping coefficients in the hybrid method, along with the drag and damping coefficients applied in all three methods, is detailed in Section 5.1 of the paper, titled "Correction Coefficient Decision.

To numerically confirm whether the three planned damping methods were well applied, comparison and validation were performed based on the time series damping motion results as shown in Fig. 1. The damping ratio (ζ) function for numerical analysis of damping is based on the logarithmic decrement (δ) for each period, calculated as follows:

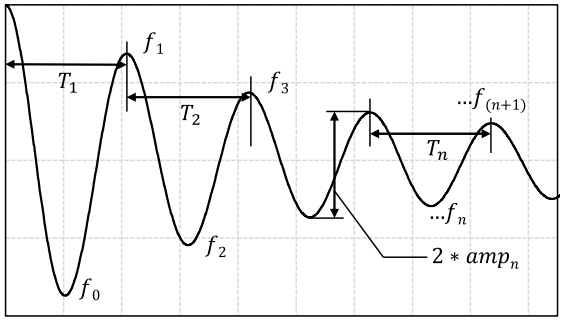

Fig. 1. Free decay motion example.

$$\delta = \ln\left(\frac{X_n}{X_{n+1}}\right) \tag{4}$$

Where X_n and X_{n+1} are two consecutive crests (e.g., $f_0 - f_2$) or troughs (e.g., $f_1 - f_3$), and the damping ratio is calculated as follows:

$$\zeta = \frac{1}{\sqrt{1 + \left(\frac{2\pi}{\delta}\right)^2}} \tag{5}$$

All load response values, such as surge, heave, and pitch, were calculated based on the sea water level. Additionally, the x and y coordinates were calculated relative to the center of the geometry of the analysis objects, when they are in a state of static equilibrium in an environment without external environmental loads. Furthermore, the surge motion was calculated with respect to the axis aligned with the direction of wave propagation.

The platform shape used in the study is shown in Fig. 2. The floater has a main column at the center where the tower and RNA (Rotor Nacelle Assembly) are attached, and three side columns are arranged at 120-degree intervals based on this. Each column is connected by an upper deck and pontoon. The properties of the floater and mooring lines required for the analysis, as well as information about the shape, are presented in Tables 1 and 2.

All damping motions were analyzed with mooring lines attached, with the fairlead position located at 12.685m above SWL and the anchor position located −150 m in the z-direction and 852.39 m away in the horizontal direction. The mentioned drag and damping coefficients were added to the potential-based analysis results, which only reflect damping effects from diffraction and radiation, as additional linear damping matrices to correct the damping.

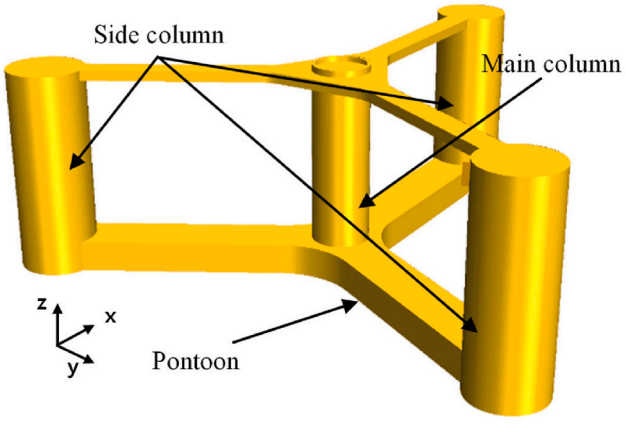

Fig. 2. Braceless 10 MW platform configuration.

Table 1
Braceless semi-submersible platform geometry information.

Geometry of platform	Value
Platform height (m)	32
Side column diameter (m)	12
Main column diameter (m)	9
Pontoon width (m)	8
Pontoon height (m)	4.8
Outer column span (m)	45
Draft (m)	15.5

Table 2
Platform and mooring properties.

Platform and mooring properties	Value
Platform mass (kg)	10,254,000
Center of mass from SWL1) (m)	−0.04, 0, 4.19
Ixx about COG (kg2 m)	1.967e10
Iyy about COG (kg2 m)	1.961e10
Izz about COG (kg2 m)	1.298e10
Displacement (m3)	10,728
Mooring upstretched length (m)	850
Mooring mass (kg/m)	162.51
Mooring stiffness (N)	1.845e6

[1)] Sea Water Level.

3. CFD verification

3.1. Free decay simulation verification

In order to obtain the necessary free decay data to determine the correction coefficient for fully coupled simulations in PBDC, CFD was utilized to verify the damping forces. Accurate determination of the correction coefficient requires verification of the CFD results. This was achieved by comparing the CFD results with the free decay experimental results from J. Palm et al. (2016), which used a cylinder-shaped model. The verification process, shown in Fig. 3, confirmed the accuracy of the CFD results.

For the simulation, the modeled cylinder had a diameter of 0.515 m and a height of 0.401 m, with a mass of 35.85 kg. The center of gravity (CoG) was set 0.0758 m above the cylinder's base, and the moments of inertia Ixx, Iyy, and Izz were set to 0.9 kg m^2, 0.9 kg m^2, and 1.18 kg m^2, respectively. The verification results, as shown in Fig. 4, demonstrate a good agreement between the experimental data and the CFD simulation.

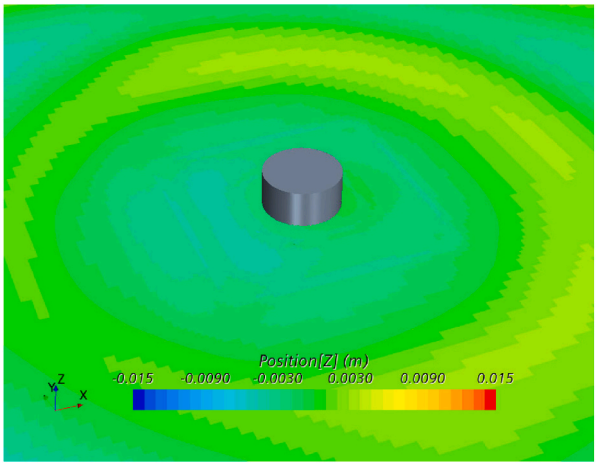

Fig. 3. Cylinder heave free decay CFD simulation.

3.2. Fully coupled simulation verification

To validate the CFD analysis for Fully Coupled FOWT under load conditions that include both wave and wind, the widely-used OC4 Semi-submersible FOWT model was utilized. The substructure and superstructure of the OC4 Semi-submersible FOWT were modeled based on the NREL reports (Robertson et al., 2014b; Jonkman et al., 2009). To account for damping effects, a Morison element was applied, and the drag coefficient required for the Morison element was referenced from the research of Wang et al. (2022c).

The analysis conditions included a first-order regular wave with a wave height of 7.58 m and a period of 12.1 s, while the wind speed was set to 11 m/s. In the CFD simulations, although the wave height was set to 7.58 m for a regular wave, factors such as temporal discretization for simulation stability, wave damping applied at the rear part of the computational domain, and the influence of the turbulence model, result in a somewhat irregular wave formation instead of the perfectly uniform wave produced by the PBDC. In cases with large wave heights, the wave height formed in the CFD might be lower than the set value depending on the simulation conditions. Since discrepancies in wave height make it difficult to compare the two codes, the wave elevation data extracted from the CFD results were applied to the PBDC for consistent comparison.

The load response comparison between the two codes for the 10 MW semi-submersible platform FOWT is presented in Fig. 5. The time series responses for surge, heave, pitch, and mooring tension were analyzed. The results indicate that when the CFD-extracted wave data were directly applied to the PBDC, the heave motion in the PBDC closely matched the heave motion observed in CFD, demonstrating a high level of agreement between the two codes. Additionally, not only heave motion but also pitch, surge motion, and mooring tension exhibited good agreement between the two codes. However, in OC4 floating structure, Potential flow theory tends to underestimate the effects of viscous force and wave force, leading to a lower surge amplitude prediction in the PBDC compared to CFD. Table 3 presents the RAO results for surge, heave, pitch, and mooring tension, providing a quantitative comparison of response amplitudes between CFD and the PBDC. The results indicate that all response components generally show good agreement between the two codes.

4. Numerical simulation method

In this study, to select the drag coefficient and damping coefficient to be used, and to analyze the calibration results of the selected coefficients, a FVM-based CFD tool was used for verification purposes. The Potential theory-based analysis tool was used to compare the results with the selected calibration coefficients applied. The descriptions of each tool are as follows.

4.1. Governing equation

To analyze the 3D flow characteristics and motion characteristics of the FOWT, the commercial FVM-based CFD program Star-CCM + developed by Siemens was used. This tool directly solves fully nonlinear, viscous fluid dynamics using the Navier-Stokes equations, so it can produce highly accurate results close to reality if appropriate grid size, grid quality, and time steps are used. In this study, considering fully coupled analysis, the flow field was considered turbulent rather than laminar, and the RANS equations, which are time-averaged forms of the continuity equation and momentum conservation equations, were used as the governing equations for the flow. The RANS approach was chosen because it provides a balance between computational efficiency and accuracy in offshore hydrodynamics and aerodynamics simulations. While Large Eddy Simulation (LES) and hybrid RANS-LES methods (e.g., Detached Eddy Simulation) can resolve more detailed turbulence structures, their computational cost is excessively high for large-scale

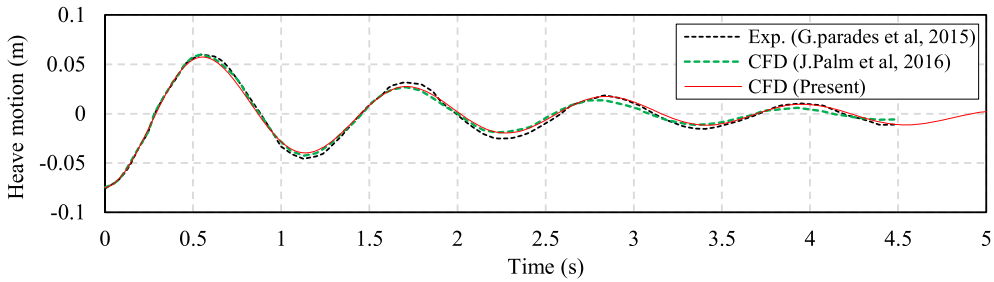

Fig. 4. Cylinder free decay result verification with CFD and experiment.

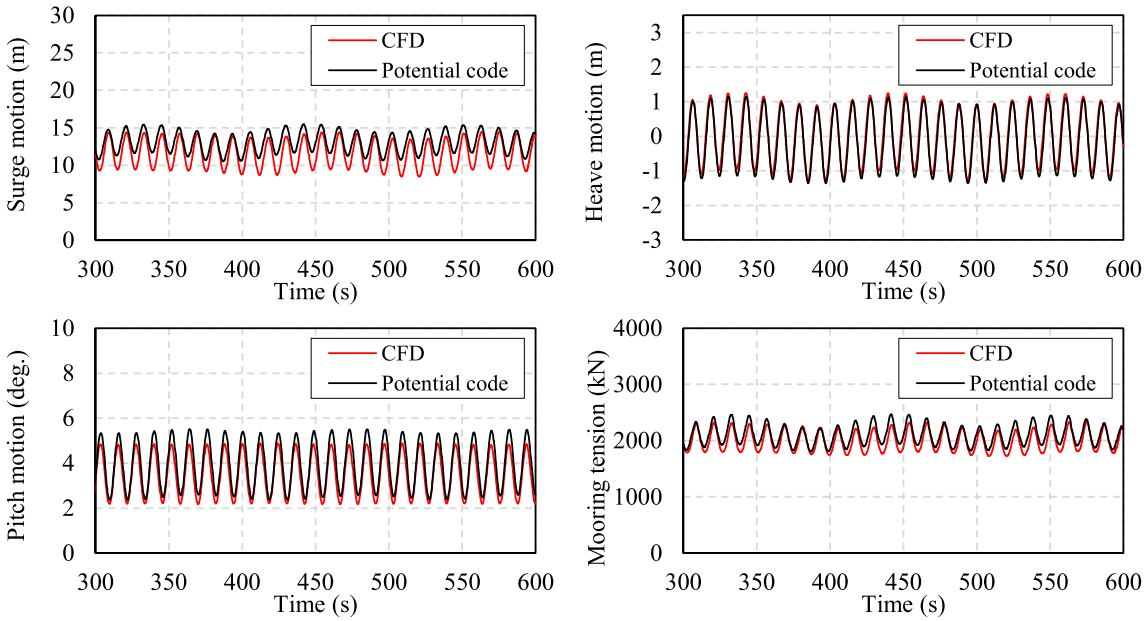

Fig. 5. OC4 DeepCwind semi-submersible FOWT fully coupled simulation comparison (Red: CFD; Black: PBDC). (For interpretation of the references to colour in this figure legend, the reader is referred to the Web version of this article.)

Table 3
OC4 FOWT RAO result for surge, heave, pitch and mooring tension.

RAOs	CFD	Potential code	Difference
Surge (m/m)	2.489	1.842	−0.647
Heave (m/m)	1.097	1.129	0.032
Pitch (deg./m)	1.321	1.477	0.156
Mooring tension (kN/m)	246.248	234.318	−11.93

FOWT simulations. Furthermore, RANS-based simulations have been validated against experimental data, demonstrating strong agreement in predicting wave-structure interactions and aerodynamic loads for floating offshore structures.

To verify the universality of the damping coefficient and drag coefficient derived from CFD simulation results, the potential-based engineering tool Orcaflex was used. Orcaflex models the interaction between waves and structures and analyzes the dynamic behavior of the structure by considering additional loads such as buoyancy, gravity, viscosity, and damping based on the modeled data. The most important wave-structure interaction modeling data was generated using Orcawave, developed by Orcina. Orcawave uses potential flow theory, assuming irrotational and incompressible flow.

4.2. Water surface modeling

Accurately satisfying the kinematic and dynamic conditions of the free surface is crucial for wave generation through numerical analysis. In the CFD used in this paper, the second-order accurate VoF method of the software was used. In this study, instead of modeling a wave generator to generate waves, the wave information obtained through wave theory was inputted into the inlet boundary, using the 1st order regular wave equation for linear waves.

The VoF model tracks the volume fraction of water and air in each cell that makes up the space. The boundary between water and air is determined based on the volume fraction value F. The Navier-Stokes equation is not applied separately for the two fluids (water and air); instead, the physical properties (such as density, viscosity, etc.) at the interface are modified according to the volume fraction by the VOF model. That is, the VOF model tracks the interface and distinguishes which phase is present in each cell, and the physical properties of that cell are calculated according to the following equations (6) and (7):

$$\rho = F \bullet \rho_{water} + (1 - F) \bullet \rho_{air} \tag{6}$$

$$\mu = F \bullet \mu_{water} + (1 - F) \bullet \mu_{air} \tag{7}$$

In this way, the physical properties change based on the value of F, and the Navier-Stokes equation applies these properties to calculate the physical phenomena. Although the VOF model can track the interface between fluids, surface tension plays a critical role at the physical boundary interface. Surface tension contributes to simulating accurate changes in the shape and waves of the free surface by calculating the additional forces occurring at the interface. The surface tension term is

added to the Navier-Stokes equation as shown in equation (8) using the curvature κ of the interface and the surface tension coefficient σ:

$$f_{st} = \sigma\kappa\mathbf{n} \tag{8}$$

Here, $\mathbf{n}$ is the unit vector normal to the surface.

The interface normal vectors were determined using the VOF model. Specifically, the normal vectors were computed as the gradient of the volume fraction field ∇F, ensuring an accurate representation of the phase boundary. This method does not require explicit surface reconstruction or matrix transformations, as the normal direction is naturally derived from the phase distribution. The computed normal vectors are further used to determine, which plays a key role in surface tension modeling within the Navier-Stokes equations.

4.3. Simulation setup

The air and water constituting the analysis space were set as incompressible fluids, with densities of 1.184 kg/m^3 and 1025 kg/m^3, respectively. The analysis was divided into free decay motion analysis and fully coupled simulation. In CFD, both analyses used the k-w SST turbulence model. The k-ω SST model was applied in this study because it is a well-validated model in offshore hydrodynamics and wind energy applications and is widely used in both industry and research. Compared to the k-ε model, the k-ω SST model offers superior performance in near-wall flow treatment and separated flow regions, enabling more accurate predictions of the flow around floating platforms and turbine structures. Additionally, it provides a good balance between computational cost and accuracy, making it widely applicable for CFD simulations of floating offshore structures. For temporal integration and discretization, a second-order numerical discretization method was used for free decay test, and a first-order method was used for fully coupled simulations. The grid was configured as shown in Figs. 6 and 7. The grid was divided into five regions: coarse, medium, fine, finer, and water surface, with grid sizes determined based on $h_{ref} = 5$ as shown in Table 4. For the free decay simulation, analysis was performed excluding the tower and RNA configuration. Considering the no wave condition of the simulation, the grid size of the water surface was approximately doubled for Δx and Δy, and quadrupled for Δx. The time step for free decay test simulation was set to 0.025 s, while for fully coupled simulation, it was set to 0.05 s to reduce analysis time. Although, errors may occur due to the increased time interval, this issue will not be addressed in this study and will be covered separately in future research. For free decay simulation, initial conditions for each motion were set to 30 m for surge, −6 m for heave, and 10° for pitch. All shapes applied to the system were considered rigid bodies. The turbine used for fully coupled simulation was the DTU 10 MW, with a rated rpm of 8.836 applied under analysis conditions based on the DTU 10 MW turbine report (Bak et al., 2013). The ideal turbine shape at this wind speed is straight, so the turbine shape was modeled as straight in the CFD analysis. The catenary method, which determines line characteristics based on anchor/fairlead position, length, mass, and stiffness, was applied to the mooring line. The same settings were applied in the potential engineering tool.

5. Results and discussion

5.1. Correction coefficient decision

The drag coefficients employed in this study are categorized based on specific zones, as illustrated in Fig. 8. These zones are delineated into three distinct regions: the column, the pontoon, and the junction where the column and pontoon intersect, with corresponding drag coefficients assigned to each. The transverse drag coefficient for the main and side columns is designated as Cds, while the transverse drag coefficient at the column-pontoon junction is denoted as Cdc. Similarly, the horizontal drag coefficient for the pontoon is represented as Cdp. Additionally, the axial drag coefficient for the column is defined as Cdcz, and the vertical drag coefficient for the pontoon is specified as Cdpz.

The drag coefficient values were determined based on experimental data and previous research findings, with Cds and Cdc set at 0.61, Cdcz at 2.4, Cdp at 3.0, and Cdpz at 2.0 (Srinivas et al., 2023; Venugopal et al., 2008). The damping coefficients were derived from free decay simulations conducted using CFD. For surge, the linear damping coefficient was set to 100 kN/(m/s), and the quadratic damping coefficient to 600 kN/(m/s)^2. For heave, the linear damping coefficient was 100 kN/(m/s), while the quadratic damping coefficient was 3000 kN/(m/s)^2. For pitch, the linear damping coefficient was set to 100e^3 kN/(m/s), and the quadratic damping coefficient to 30e^6 kN/(m/s)^2. In the hybrid calibration approach combining both drag and damping coefficients, the same drag coefficient values were applied. The damping coefficients for the hybrid method were calibrated by comparing results from simulations using only drag coefficients with those incorporating CFD-derived damping coefficients. This comparison identified regions of excessive or insufficient damping during the decay period, which informed subsequent adjustments. The damping coefficient used in the hybrid method was calibrated by minimizing the discrepancies between the crest and trough amplitudes observed in the CFD free decay motion and their corresponding time intervals. To facilitate this calibration, the ranges for the linear and quadratic damping coefficients were defined for each DoF, as detailed in Table 5. Within these predefined ranges, the coefficients were systematically varied at regular intervals, and parametric studies were conducted to evaluate their effects.

In the potential model, interactions between individual DOFs are

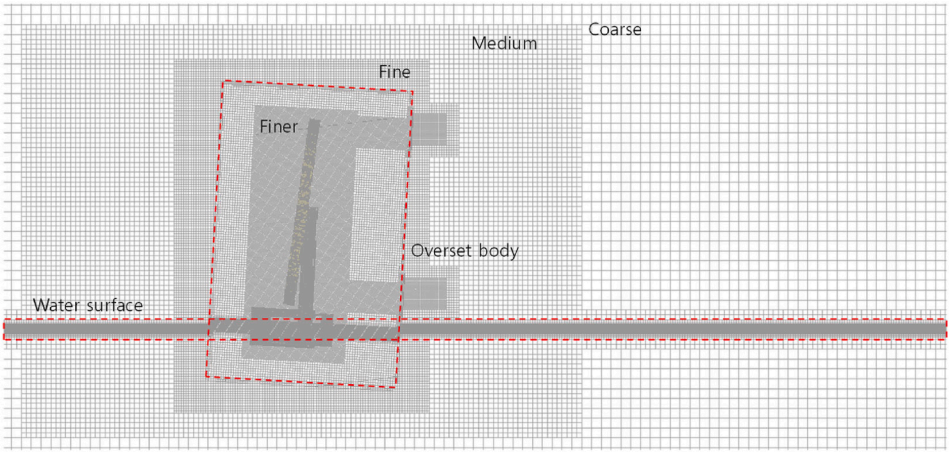

Fig. 6. Grid composition for FOWT simulation.

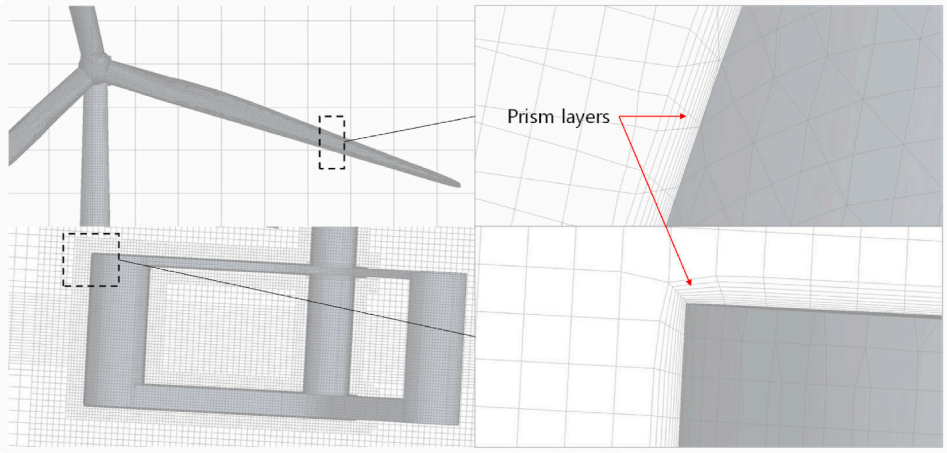

Fig. 7. Overset zone grid composition (detail).

Table 4
Mesh size and prism layer characteristics by spatial zone.

	$\Delta x/h_{ref}$ (−)	$\Delta y/h_{ref}$ (−)	$\Delta z/h_{ref}$ (−)	Prism layers		
				No. Of layers (−)	Stretching (−)	Thickness (m)
Coarse zone	2	2	2	–	–	–
Medium zone	1	1	1	–	–	–
Fine zone	0.5	0.5	0.5	–	–	–
Finer zone	0.25	0.25	0.25	–	–	–
Water surface zone	0.5	0.5	0.25	–	–	–
Platform	0.125	0.125	0.125	10	1.2	0.4
Tower & Nacelle	0.125	0.125	0.125	10	1.2	0.4
Blade	0.04	0.04	0.04	10	1.2	0.1

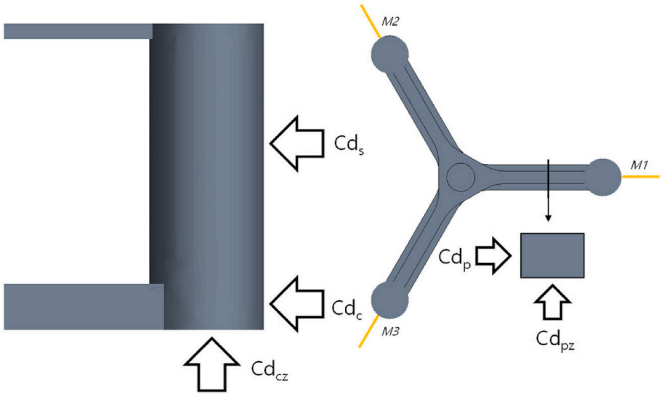

Fig. 8. Distribution of drag coefficient of platform.

Table 5
Damping coefficient variables for correction coefficient decision study.

Damping Coefficient	DoF	Unit	Range of value	Discrete spacing
Linear	Surge	[kN/(m/s)]	[10,190]	20
	Heave	[kN/(m/s)]	[0180]	20
	Pitch	[kN/(rad/s)]	[0 450 × 10^3]	50e3
Quadratic	Surge	[kN/(m/s)^2]	[-800 1000]	200
	Heave	[kN/(m/s)^2]	[-2000 2500]	500
	Pitch	[kN/(rad/s)^2]	[-40 × 10^6 50 × 10^6]	10e6

minimal, allowing the analysis of each DOF to be conducted independently. However, a comprehensive analysis was performed with all DOFs coupled. A total of 300 simulations were conducted: 100 surge free-decay simulations to evaluate the surge damping coefficient, 100 heave free-decay simulations for the heave damping coefficient, and 100 pitch free-decay simulations for the pitch damping coefficient. The determination of the surge damping coefficient involved comparing the time gap $t_{period\ gap}$, between the two models using Equation (9), and the peak value gap, $v_{peak\ gap}$, using Equation (10).

For heave and pitch, the response period is shorter than that of surge, so the initial region was excluded from the analysis to focus on more stabilized motion. Additionally, as time progresses, the effect of radiated irregular energy increases, leading to greater discrepancies between the simplified PBDC and the CFD in the later stages. To avoid this, the damping coefficients for heave and pitch were determined using data from the second cycle up to 200 s, comparing the time gap $t^*_{period\ gap}$ and peak value gap $v^*_{peak\ gap}$ using Equations (11) and (12). The results of the gap analysis for the damping coefficients are shown in Figs. 9–11.

The period gap analysis was conducted based on the percentage of the response period for each DoF of the platform. Based on the analysis, the surge damping coefficient for the hybrid method was determined to be a linear damping coefficient of 130 kN/(m/s) and a quadratic damping coefficient of −400 kN/(m/s)^2. The heave damping coefficient was set to a linear damping coefficient of 0 kN/(m/s) and a quadratic damping coefficient of 1500 kN/(m/s)^2, while the pitch damping coefficient was determined to be a linear damping coefficient of 0 kN/(rad/s) and a quadratic damping coefficient of -2e7 kN/(rad/s)^2. To achieve a balanced damping response and reduce excessive damping effects, a negative quadratic damping coefficient was applied to some DoFs. During the initial correction process, after applying the drag coefficient, it was observed that the PBDC exhibited greater damping than the CFD results. To address this, a negative quadratic damping coefficient was

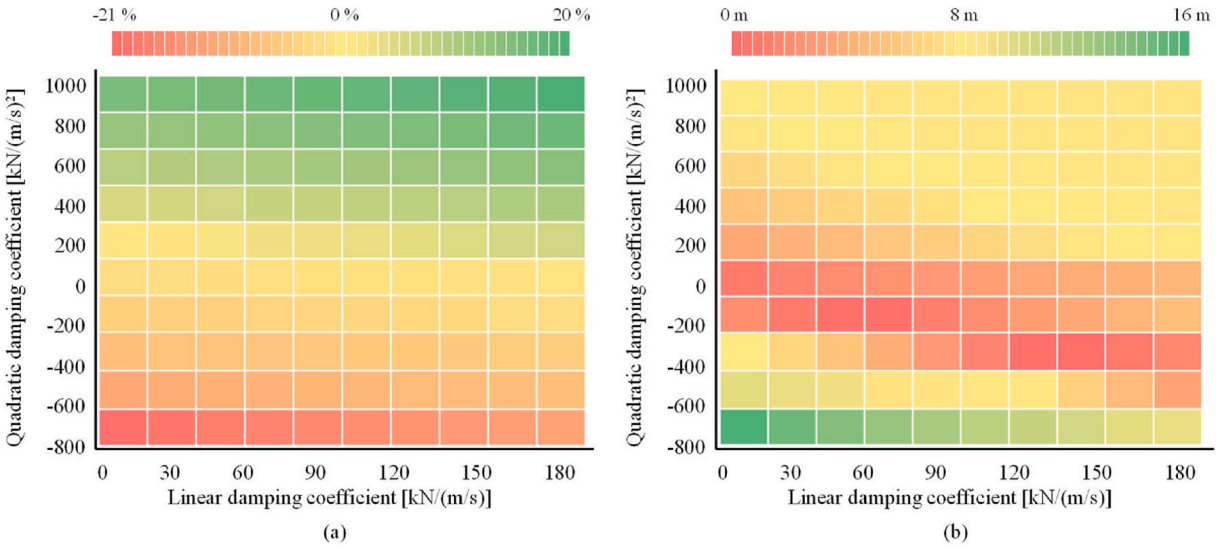

Fig. 9. CFD and potential surge decay gap analysis study (a: period gap analysis, b: peak gap analysis).

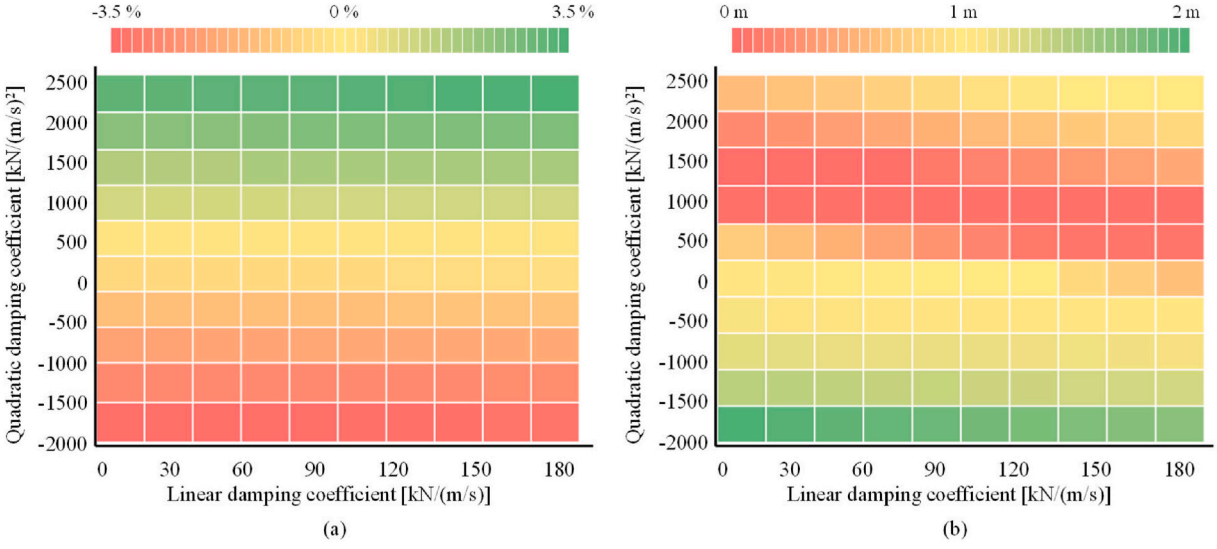

Fig. 10. CFD and potential heave decay gap analysis study (a: period gap analysis, b: peak gap analysis).

introduced to align the damping response of the PBDC with the CFD free decay test results, effectively mitigating excessive damping effects and achieving a more balanced response.

$$t_{period\ gap} = \frac{\sum_{1}^{n}\left(t_{CFD\ crest\ n} - t_{Potential\ crest\ n}\right) + \sum_{1}^{n}\left(t_{CFD\ trough\ n} - t_{Potential\ trough\ n}\right)}{2n} \tag{9}$$

$$v_{peak\ gap} = \frac{\sum_{1}^{n}\left|Crest_{CFD\ t_n} - Crest_{Potential\ t_n}\right| + \sum_{1}^{n}\left|Trough_{CFD\ t_n} - Trough_{Potential\ t_n}\right|}{2n} \tag{10}$$

$$t^{*}_{period\ gap} = \frac{\sum_{2}^{n^{*}}\left(t_{CFD\ crest\ n} - t_{Potential\ crest\ n}\right) + \sum_{2}^{n^{*}}\left(t_{CFD\ trough\ n} - t_{Potential\ trough\ n}\right)}{2n} \tag{11}$$

$$v^{*}_{peak\ gap} = \frac{\sum_{2}^{n^{*}}\left|Crest_{CFD\ t_n} - Crest_{Potential\ t_n}\right| + \sum_{2}^{n^{*}}\left|Trough_{CFD\ t_n} - Trough_{Potential\ t_n}\right|}{2n} \tag{12}$$

5.2. Calibration of hydrodynamic correction coefficient

The outcomes of the free decay simulation are presented in Fig. 12 and Table 6. Due to their similarity to the M2 results, the tension data for M3 were excluded from the analysis. The simulation focused solely on the platform, offset by 30 m in the surge direction, and examined the time-series load results at the fairlead resulting from the decay motion. A comparison of results from the CFD model and the Potential flow tool indicates that the pre-tension for M1 was −2.4 % and for M2 was −0.82 %, demonstrating strong agreement between the two methodologies. The peak tension was observed during the first damping interval for both M1 and M2. For M1, the Potential tool simulation corrected only by Morison yielded the lowest deviation at −7.08 %, followed by −3.98 % for the damping model and −1.65 % for the hybrid model. Among these, the hybrid model predicted peak tension most closely matching the CFD

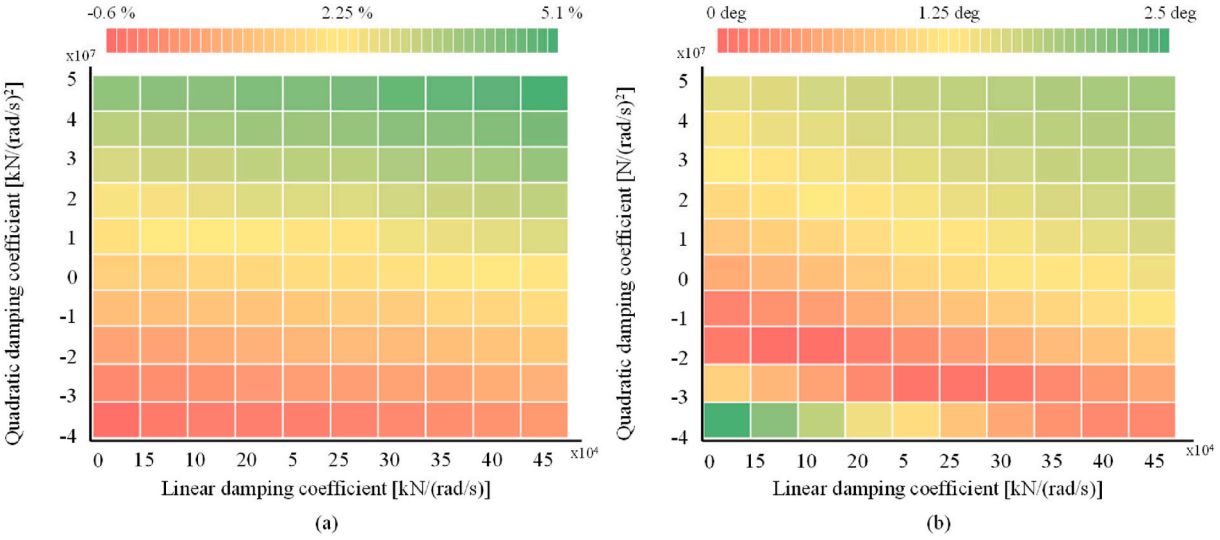

Fig. 11. CFD and potential pitch decay gap analysis study (a: period gap analysis, b: peak gap analysis).

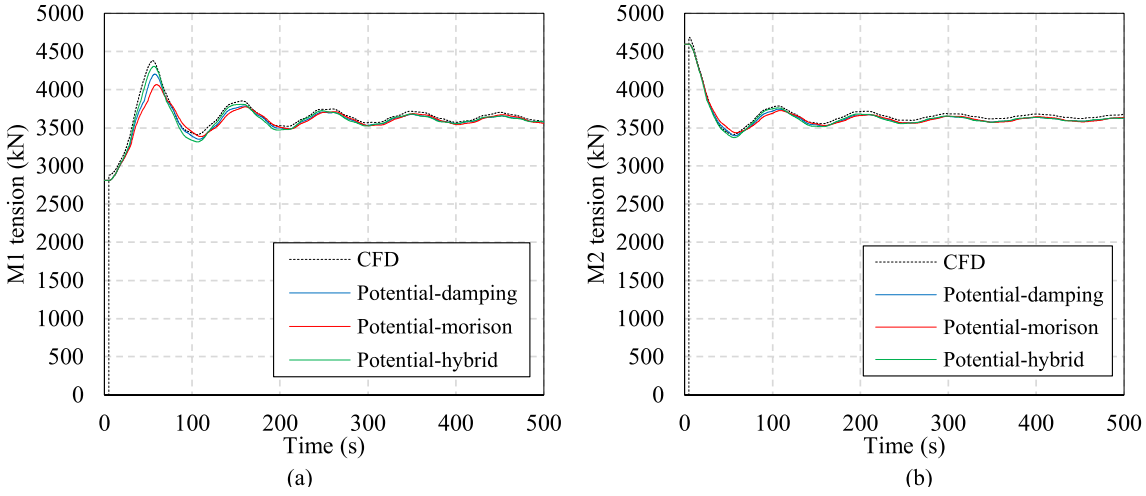

Fig. 12. Free decay simulation time series result (a: M1 fairlead tension, b: M2 fairlead tension).

Table 6
Free decay simulation mooring line tension result.

		CFD	Potential-damping		Potential-morison		Potential-hybrid	
		Value (kN)	Value (kN)	Error (%)	Value (kN)	Error (%)	Value (kN)	Error (%)
M1	Pretension	2879	2810	−2.40 %	2810	−2.40 %	2810	−2.40 %
	Maximum	4376	4202	−3.98 %	4066	−7.08 %	4304	−1.65 %
	Quasi-equilibrium state	3638	3608	−0.82 %	3608	−0.82 %	3609	−0.80 %
M2	Pretension	4686	4596	−1.92 %	4596	−1.92 %	4596	−1.92 %
	Maximum	3755	3744	−0.29 %	3724	−0.83 %	3760	0.13 %
	Quasi-equilibrium state	3650	3610	−1.10 %	3610	−1.10 %	3610	−1.10 %

results. Damping was simulated over a 500-s period, and although complete stabilization was not achieved within this timeframe, the average tension in the quasi-equilibrium state, defined between 300 and 500 s, was assessed. For both M1 and M2, the tension discrepancy between the CFD and the Potential engineering tool was minimal, at approximately 1 % or less, confirming that the two methods exhibit a high degree of consistency in tension performance prediction.

Fig. 13 presents the time series results of the free decay simulation for 3DoF motions: (a) surge, (b) pitch, and (c) heave. The simulations were conducted with all six DoFs free during the decay motion. An analysis of the time series results reveals that the Potential engineering tool demonstrates good agreement with the free decay simulations performed using CFD, irrespective of the calibration method employed. For a more detailed evaluation, the crest and trough values of each motion's decay simulation were compared and analyzed, as illustrated in Figs. 15–17.

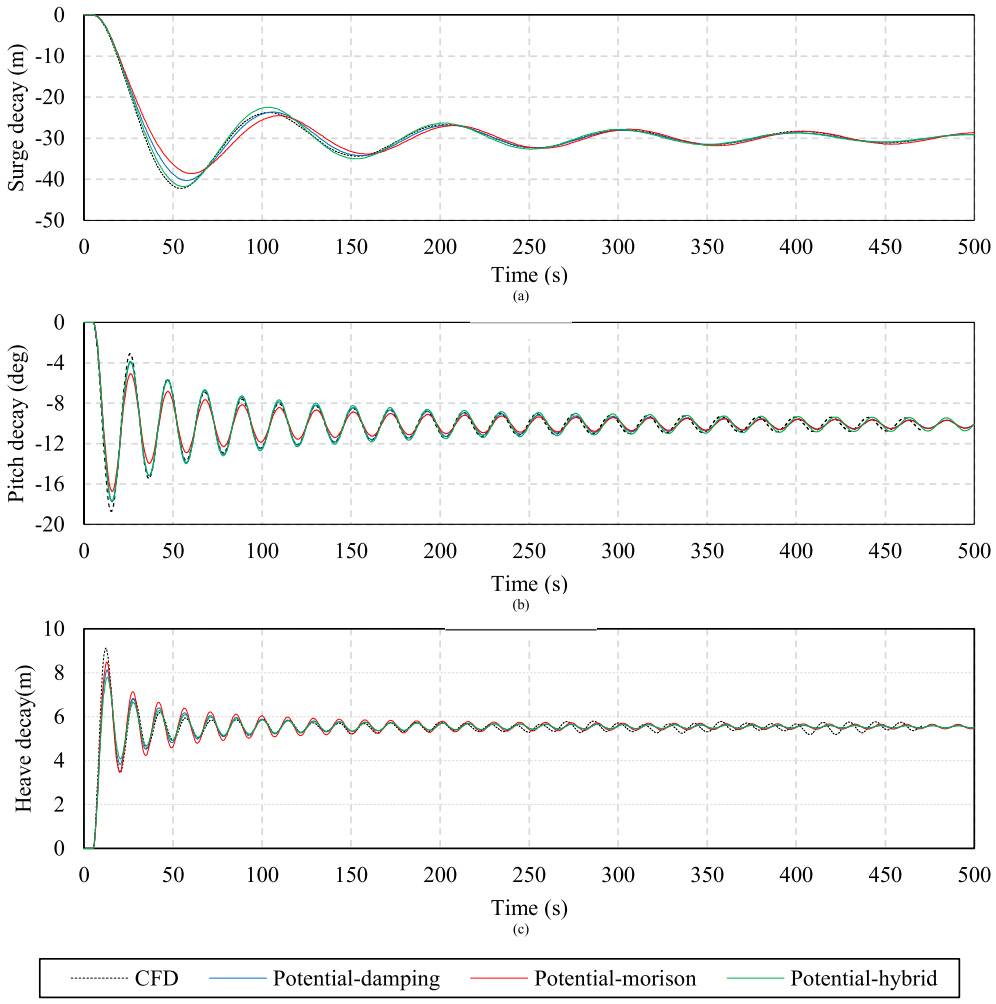

Fig. 13. Free decay simulation time series result (a: Surge, b: Pitch, c: Heave).

Analyzing the surge free decay test results presented in Fig. 14, the calibration method based on the damping coefficient exhibited minimal deviation from the CFD data for the crest during the first damping interval, whereas the calibration using only the drag coefficient showed a discrepancy of approximately ±1 m. When evaluated as a percentage difference per interval, this corresponded to about 10 %. In subsequent intervals, all calibration methods aligned closely with the CFD results. However, during the final damping interval, the damping coefficient-based calibration deviated by −0.5 m from the CFD, equating to a −30 % difference rate. For the trough in the first interval, the damping coefficient-based calibration showed a value of 2 m, while the drag coefficient-based calibration recorded 3.5 m, with respective percentage differences of 25 % and 50 %. Despite these initial discrepancies, the methods demonstrated strong agreement with CFD results in the remaining intervals.

Analyzing the pitch free decay results presented in Fig. 15 reveals discrepancies between the drag coefficient values derived from reference data and those observed in reality. Notably, the crest and trough heights exhibit significant deviations from the CFD predictions in most damping intervals when calibrated solely using the drag coefficient, compared to other calibration approaches. These deviations are particularly pronounced in the first damping interval, both numerically and in terms of height. Calibration based solely on the damping coefficient yielded reasonable agreement across the damping intervals; however, similar to the surge results, the differences became markedly larger in the later intervals. In contrast, the hybrid calibration method demonstrated superior accuracy in predicting the pitch free decay motion across all intervals compared to the other methods.

Fig. 16 presents the results of the heave free decay analysis. In the later stages of the oscillation, the amplitude of the motion was minimal, leading to relatively high error rates in these intervals. To address this, the heave decay motion was evaluated using the simple numerical differences between the crest and trough. During the initial interval, both the damping and hybrid methods exhibited notable errors; however, in subsequent intervals, they demonstrated improved agreement compared to the Morison method, with the hybrid method showing the closest alignment. From the mid to late intervals, all methods exhibited comparable trends with significant variations. These differences were attributed to the small-amplitude heave motion observed in the CFD analysis, which generated complex flow patterns and irregular motion, diverging from the predictions of potential-based simulations.

Fig. 17 presents an analysis of free decay simulations, focusing on the damping ratio as a function of amplitude and period. The results are compared across CFD simulations and a potential engineering tool. Fig. 17(a) and (b) illustrate the surge free decay simulation outcomes, demonstrating strong agreement with the CFD results. Among the methods evaluated, the hybrid approach showed the closest alignment with CFD predictions across all oscillation and period intervals. Fig. 17 (c) and (d) depict the pitch free decay simulation results. While the Morison method exhibited slightly higher deviations in the damping ratio as a function of amplitude compared to other methods, it was most consistent with the CFD predictions during the initial damping interval of the period analysis. The other two methods yielded similar results, with all approaches showing good overall agreement with CFD data in

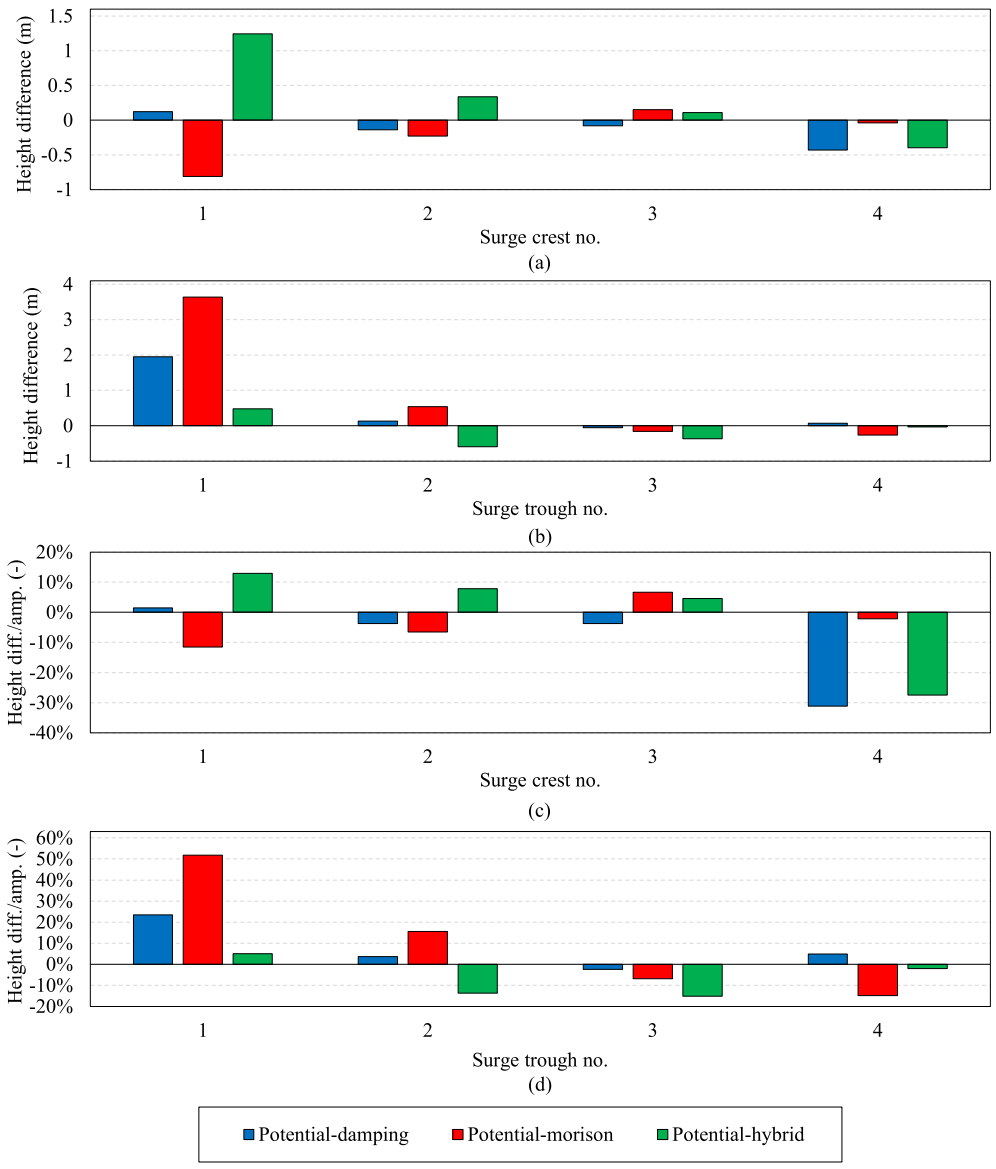

Fig. 14. Surge free decay simulation: crest and trough difference results according to correction method.

the full damping interval. Fig. 17(e) and (f) report the heave free decay simulation results. Except for a small interval where the measured amplitude was less than 0.5 m, the three correction methods generally predicted damping ratios similar to the CFD results. In cases where amplitudes were below 0.5 m, the damping ratio converged to nearly zero. This convergence reflects irregularities influenced by wave effects generated by motion rather than the inherent heave dynamics, resulting in outliers in the CFD damping ratio. However, as heave motions of such small amplitude are not anticipated in the load cases analyzed, this effect was deemed negligible. Overall, the results affirm that the evaluated methods provide reliable predictions of damping ratios in comparison to CFD, with notable variations explained by physical phenomena and methodological differences in specific cases.

Fig. 18 presents the period results obtained from analyzing the time intervals between successive troughs and crests observed in the free decay simulations for surge, pitch, and heave motions. Each free decay analysis was conducted over the same time duration, yielding approximately 7 data points for surge, 45 for pitch, and 66 for heave. The results reveal that the periods estimated using CFD exhibited greater variability compared to those derived from the potential flow method across all decay motions. Specifically, in the surge free decay, the potential flow method demonstrated a maximum period deviation of approximately 1 s, while the CFD results showed a deviation of up to 4 s. The average period difference between the two methods was about 1 s, which corresponds to roughly 1 % of the natural period, estimated to be around 99 s. For pitch and heave, the natural periods observed in the CFD analysis showed smaller deviations compared to surge. The potential flow method, in contrast, exhibited negligible deviation in these motions. The average differences between the two methods for pitch and heave were less than 0.1 s, translating to differences of under 1 %. Overall, the comparative analysis confirms that the differences in natural periods for the 3DoF motions between the two methods remain within 1 %.

5.3. *Fully coupled simulation*

An integrated load analysis was conducted utilizing a potential analysis tool in conjunction with three selected calibration methods and CFD. The study evaluated performance under two distinct environmental scenarios: rated wind conditions and cut-out wind conditions. Both scenarios assumed a water depth of 150 m, with air and water densities set to 1.184 kg/m^3 and 1025 kg/m^3, respectively. For the rated

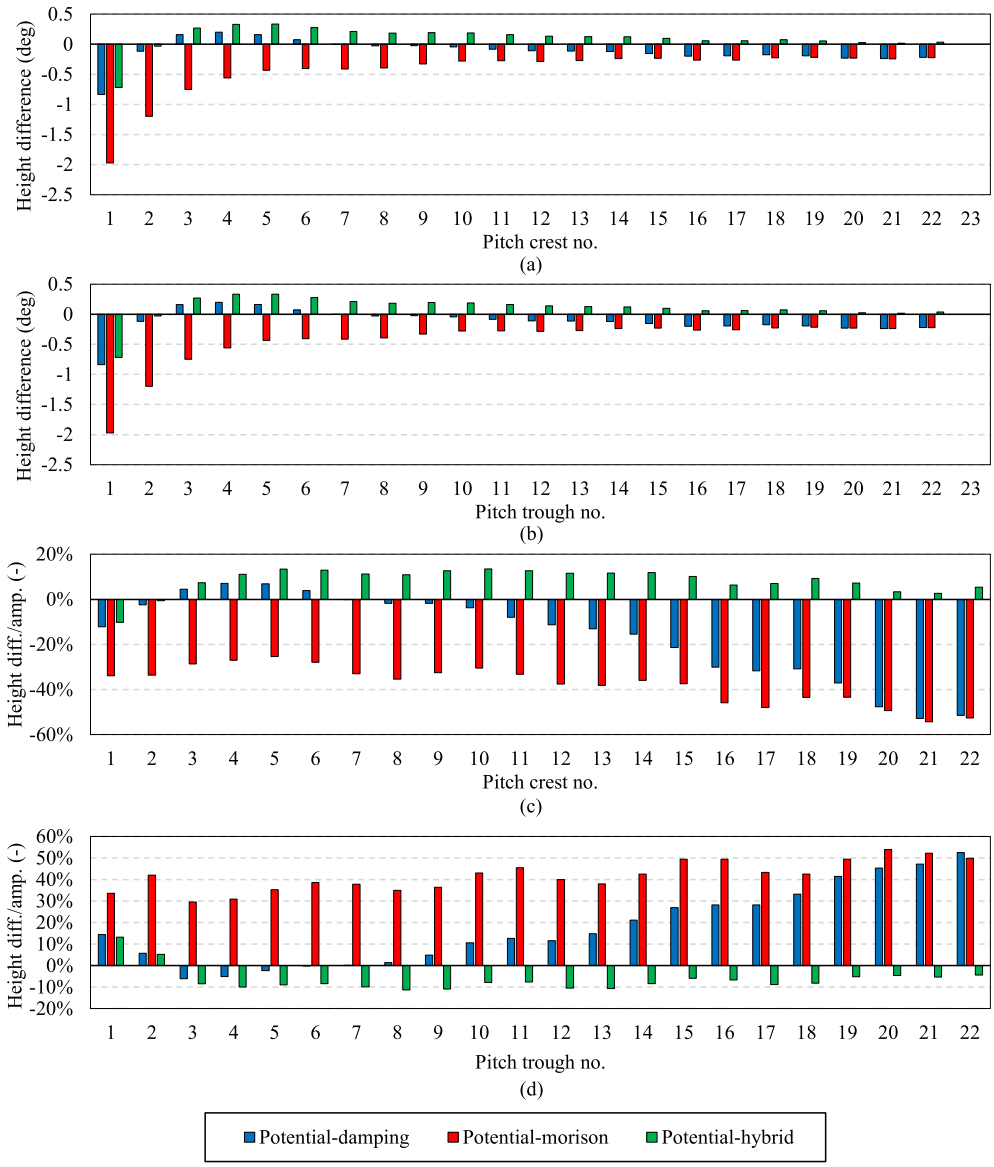

Fig. 15. Pitch free decay simulation: crest and trough difference results according to correction method.

wind conditions, a steady wind speed of 11 m/s, free from turbulence or power-law effects, was applied, along with a wave height of 6.0 m and a wave period of 10 s for CFD simulations. Under cut-out wind conditions, the wind speed was increased to 24.0 m/s, with a wave height of 6.14 m and a wave period of 13.0 s. When applying the wave model, the difference in wave profile accuracy between the first-order wave model and higher-order wave models was insignificant in low wave height conditions. Additionally, while higher-order wave models provide greater accuracy, they also have a higher risk of numerical divergence and discretization errors when coupled with a turbulence model. Considering these factors, the first-order wave model was chosen instead of the fifth-order wave model for the fully coupled simulation. As discussed in the CFD validation section, the simulations performed in this study revealed wave height attenuation within the region of interest. This attenuation was attributed to factors such as temporal discretization, wave damping at the rear boundary of the computational domain, and the turbulence model employed. To enable a precise comparison between the computational codes, it was essential to harmonize the environmental conditions. To achieve this, wave data derived from the CFD simulations were utilized as input for the PBDC, ensuring maximum consistency in environmental conditions. Subsequently, the reconstructed wave data were applied to the PBDC under the specified load conditions.

5.3.1. *Rated wind condition*

Figs. 19–21 present the outcomes of an integrated load analysis conducted under rated wind conditions, employing CFD and a PBDC. These results include the time series of three DoF motion, aerodynamic performance, and mooring fairlead tension. The mean drift, average values, and oscillation amplitudes for each load parameter are summarized in Tables 7–9. Fig. 19(a) displays the time series of surge motion, where the periodic behavior predicted by the PBDC aligns closely with the CFD results. However, all three correction methods slightly underpredict the responses, with the mean surge drift differing by approximately 2 m, representing an underestimation of about 7–8 %. Fig. 19(b) illustrates the heave motion response, showing excellent agreement between the CFD results and the correction methods applied in the PBDC. As summarized in Table 7, the errors in the mean values and amplitudes of heave motion are within 0.05 m, which are considered negligible. Fig. 19(c) depicts the pitch motion, where the predicted periods align well between the CFD and all correction methods. Nevertheless, slight discrepancies in the mean values are observed across the

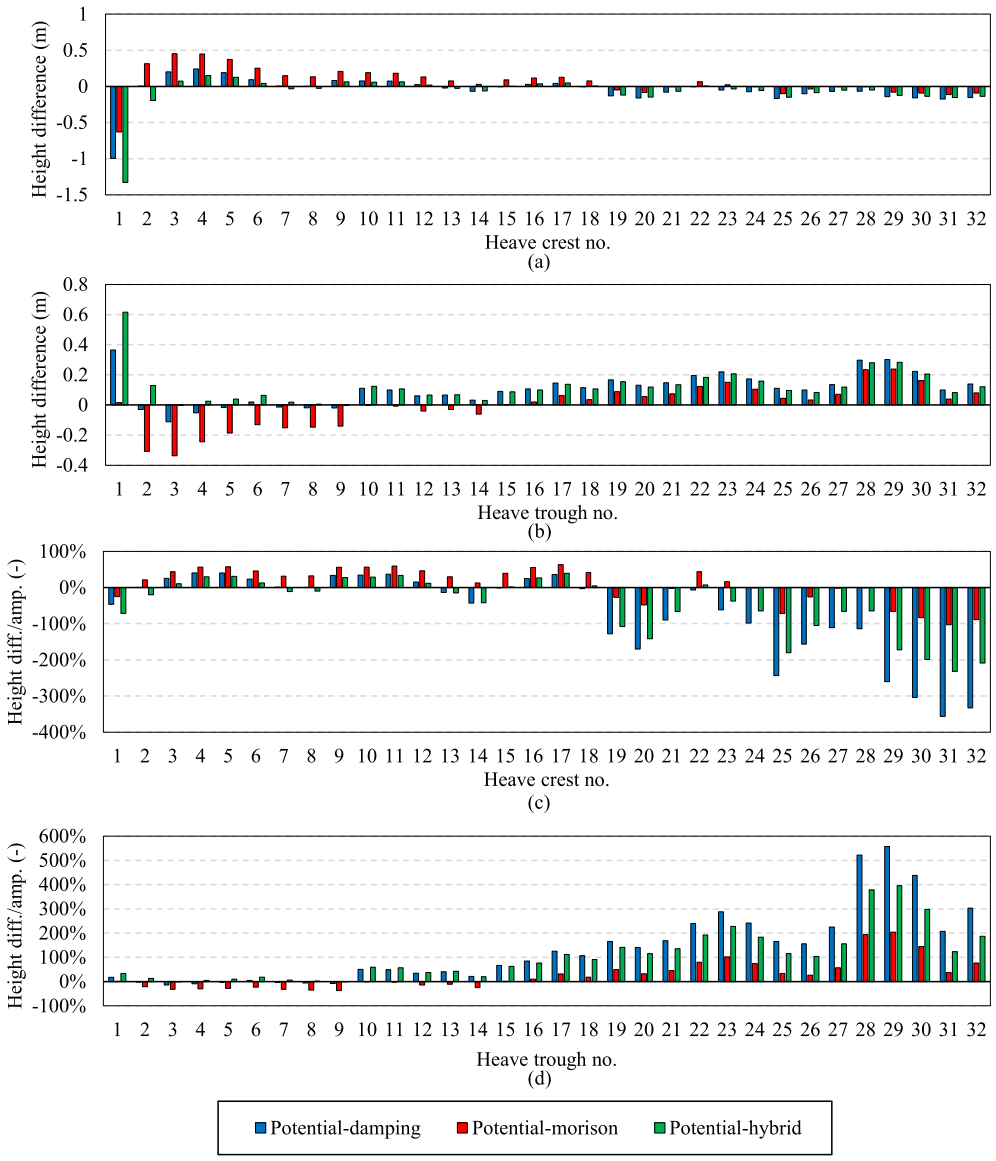

Fig. 16. Heave free decay simulation: crest and trough difference results according to correction method.

methods. Table 7 indicates that the damping method overestimates the mean pitch by approximately 3.13 %, while the Morison and hybrid methods demonstrate higher accuracy, with errors of about 1.42 %. The differences in oscillation amplitude relative to CFD predictions across all methods remain within 0.1°.

Fig. 20 illustrates the time series of the aerodynamic performance of the turbine under rated wind conditions. Consistent with the three DoF motion responses, the thrust and torque responses show excellent agreement with CFD results, both in terms of amplitude and mean values, across all correction methods. Phase differences in aerodynamic performance are attributed to the combined effects of motions such as surge, sway, and pitch. These interdependencies in system response phases between the codes contribute to variations in aerodynamic performance phases. Consequently, the findings demonstrate that the PBDC and the correction methods employed in this study not only accurately predict aerodynamic and hydrodynamic behavior but also effectively capture the interplay between these dynamic phenomena. The observed abrupt inversions in torque and thrust occur due to the Tower Shadow Effect, which happens when rotor blades pass in front of the tower. As the blades enter the tower wake region, they experience a temporary reduction in aerodynamic force due to flow blockage and wake effects, leading to a sudden drop in aerodynamic torque followed by a recovery. This periodic pattern is a well-known physical phenomenon in floating offshore wind turbines. A frequency analysis confirms that these fluctuations correspond to the blade passing period (1P), which is approximately 2 s. Therefore, the torque variations observed in this study are identified as a physical response caused by tower wake interactions, rather than numerical artifacts. Furthermore, this behavior was consistently captured in both CFD and potential flow models.

Table 8 reveals that the average thrust values estimated by the three correction methods align closely with the CFD results, differing by approximately 3 %, while the oscillation amplitude shows a deviation within 20 kN. Likewise, the torque predictions for all three methods exhibit average values within 3 % of the CFD results, underscoring their high degree of accuracy.

The load response of mooring line tension is illustrated in Fig. 21 and summarized in Table 9. Under the applied load conditions, the tension response of the mooring lines is predominantly governed by the surge motion. Mooring line M1, which is directly influenced by surge dynamics, exhibited a response error of approximately 7 % across all correction methods, aligning with the discrepancies observed in the surge response. In terms of oscillation amplitude, the PBDC predicted

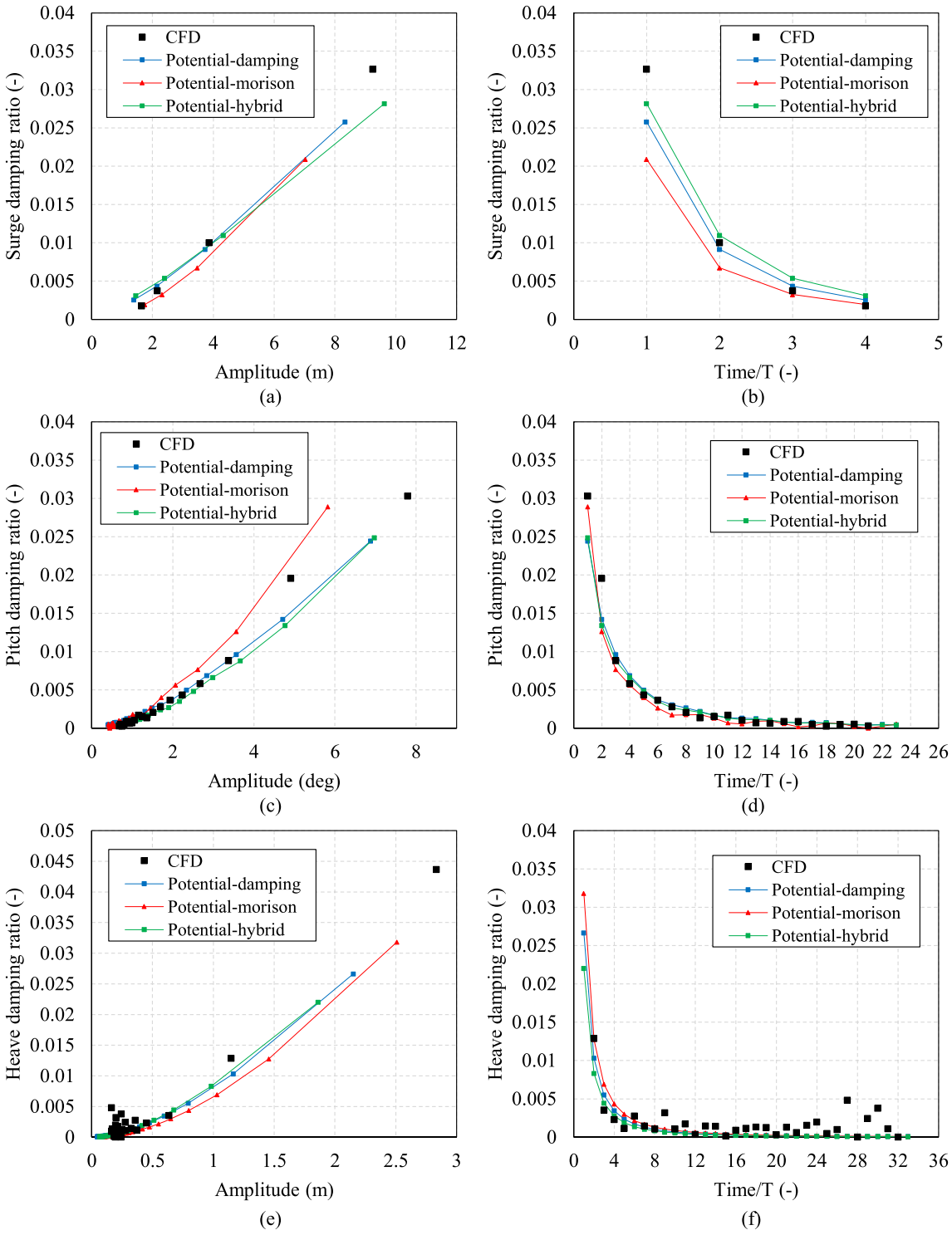

Fig. 17. 3DoF damping ration according to amplitude and period.

slightly lower values for M1, with deviations of approximately 50 kN compared to the CFD results. Conversely, mooring lines M2 and M3, which are less sensitive to surge motion, demonstrated minimal differences in average response compared to CFD, with deviations below 2 % across all correction methods in the PBDC. Amplitude differences for M2 and M3 were within 1 kN, indicating a high degree of accuracy in the predicted mooring response. These results underscore the effectiveness of the applied correction methods in accurately capturing mooring line behavior under the investigated conditions.

5.3.2. *Cut-out wind condition*

The results of the analysis for the cut-out wind condition, conducted using CFD and a PBDC incorporating three correction methods, are detailed in Figs. 22–24 and Tables 10–12. In contrast to the previous configuration, this analysis employed mooring lines approximately 2.5 times heavier than the original ones to examine the effects of increased mooring line loads on the load response. The environmental conditions corresponded to a cut-out wind scenario, characterized by a wind speed of 24 m/s and a turbine rotation rate of 9.6 rpm. For the DTU 10 MW turbine, the pitch angle typically adjusts to regulate loads and optimize

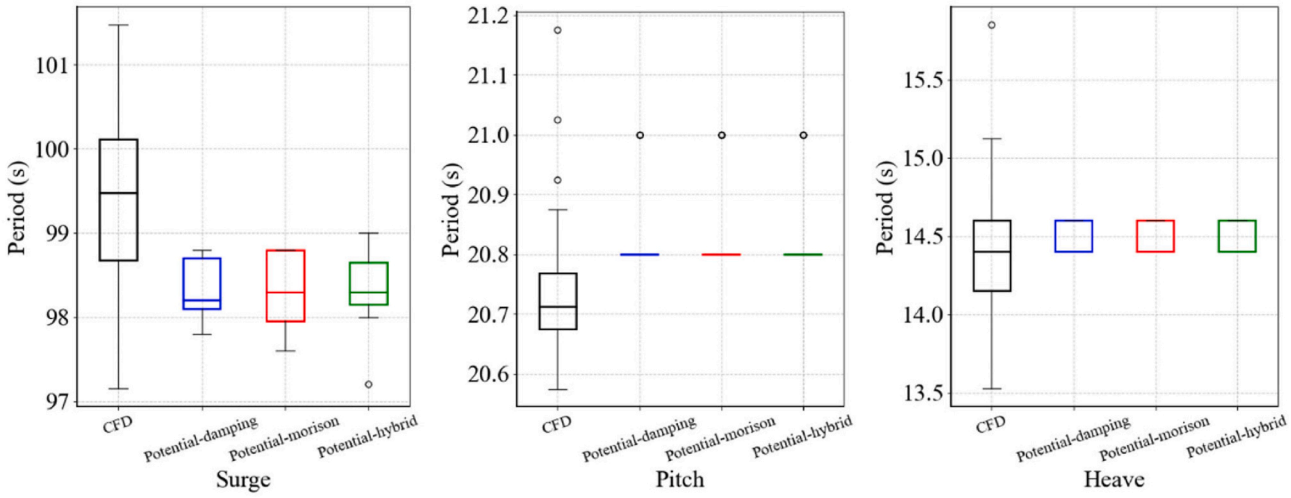

Fig. 18. Comparison of natural period of CFD and different correction coefficient adapted potential based engineering tools (left: surge natural period, middle: pitch natural period, right: heave natural period).

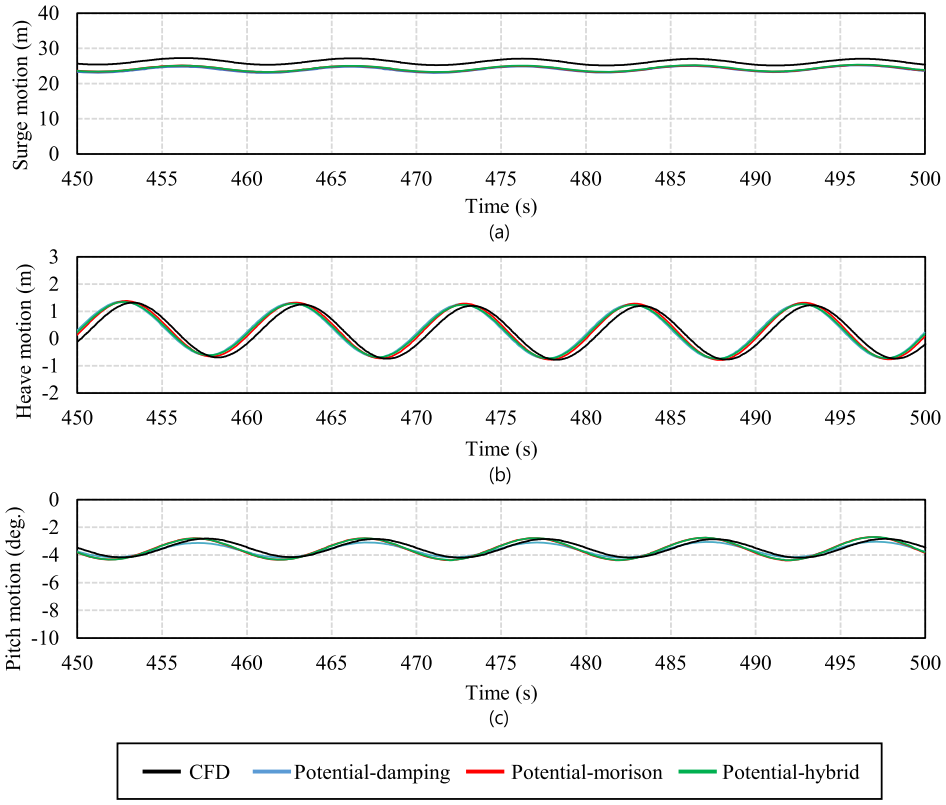

Fig. 19. FOWT 3DoF response result with rated wind and regular wave condition.

performance when wind speeds exceed the rated threshold of 11 m/s. However, in this study, the pitch angle was intentionally fixed at 0° to assess the capability of the integrated load analysis in predicting turbine loads under non-standard operating conditions and high structural loads. Consequently, torque analysis was excluded from the aerodynamic evaluation, as the fixed pitch angle does not account for realistic operational adjustments at high wind speeds. The study therefore focused exclusively on thrust as the primary aerodynamic parameter.

Fig. 22(a) illustrates the temporal surge response, highlighting that, despite increased loads on the mooring lines and upper structure compared to previous conditions, the PBDC, incorporating all correction methods, accurately predicted the mean surge drift and oscillation amplitudes in close agreement with CFD results. Fig. 22(b) presents the time-series response of heave motion, comparing CFD predictions with those from the PBDC. The Morison and Hybrid methods exhibited strong concordance with CFD, while the Damping method displayed notable phase discrepancies and reduced amplitude predictions. Fig. 22(c) shows the pitch motion response, revealing a consistent trend with the previous two motions. While the Morison and Hybrid methods achieved high fidelity with CFD predictions, the Damping method exhibited significant deviations, failing to capture the overall dynamic characteristics of the pitch response. Table 10 presents a comparison of the mean values

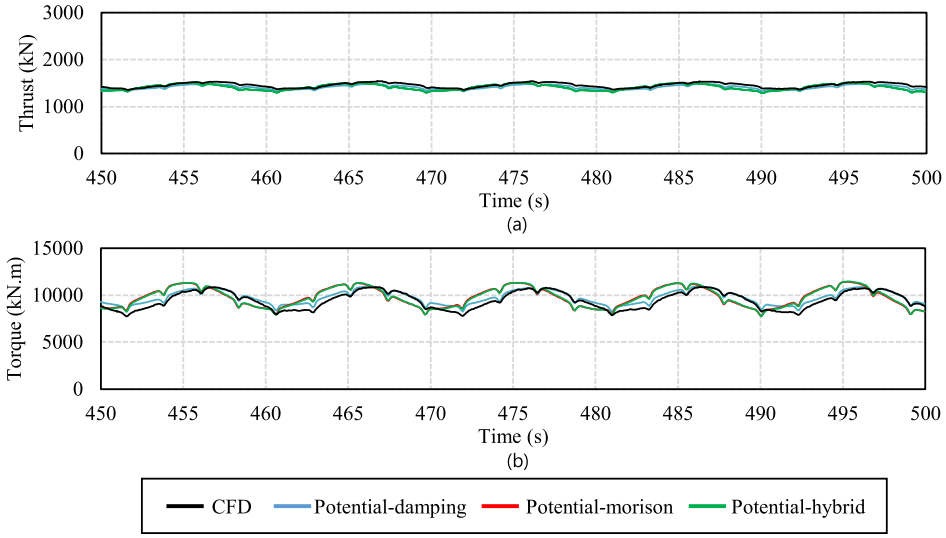

Fig. 20. FOWT aerodynamic performance result with rated wind and regular wave condition.

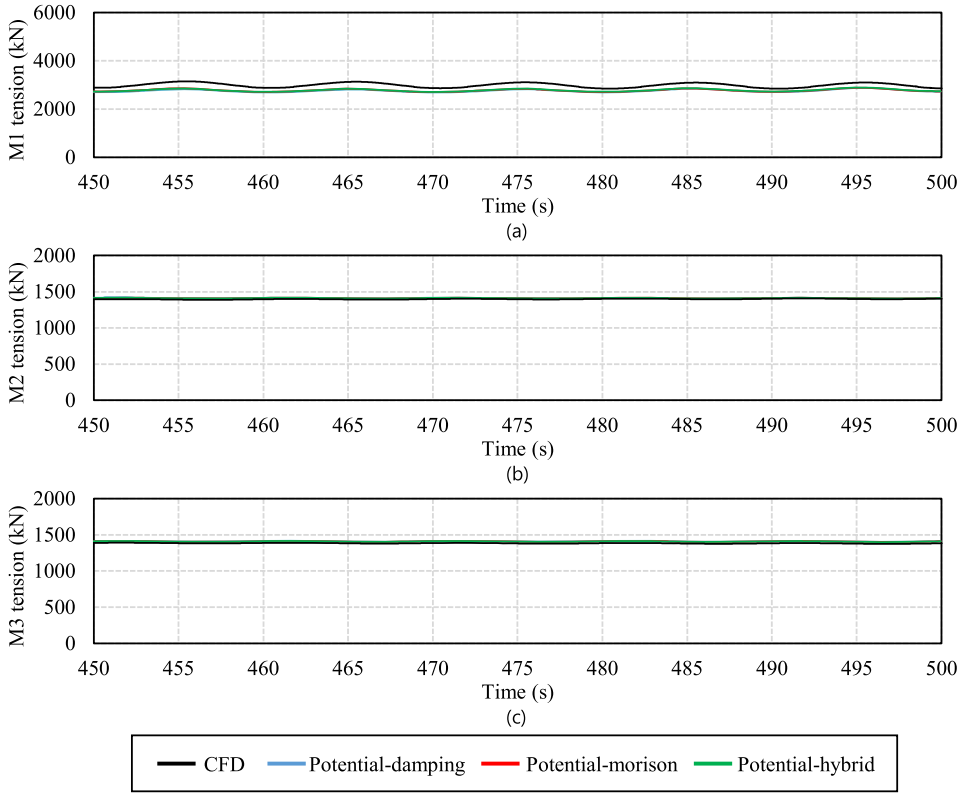

Fig. 21. FOWT mooring tension result with rated wind and regular wave condition.

Table 7
FOWT 3DoF mean drift and oscillation amplitude comparison in rated wind and regular wave condition.

	Surge				Heave				Pitch			
	Mean drift (m)	Mean diff. (%)	Amp. (m)	Amp diff. (m)	Mean drift (m)	Mean diff. (%)	Amp. (m)	Amp diff. (m)	Mean drift (deg.)	Mean diff. (%)	Amp. (deg.)	Amp diff. (deg.)
CFD	26.19	–	0.93	–	0.24	–	0.99	–	−3.51	–	0.67	–
Damping	24.02	−8.29	0.90	−0.03	0.29	20.83	0.99	0	−3.62	3.13	0.54	−0.13
Morison	24.22	−7.52	0.90	−0.03	0.29	20.83	1.01	0.02	−3.56	1.42	0.79	0.12
Hybrid	24.27	−7.33	0.90	−0.03	0.29	20.83	0.98	−0.01	−3.56	1.42	0.78	0.11

Table 8
FOWT aerodynamic performance average value and oscillation amplitude comparison in rated wind and regular wave condition.

	Thrust				Torque			
	Average (kN)	Avg diff. (%)	Amp. (kN)	Amp diff. (kN)	Average (kN-m)	Avg diff. (%)	Amp. (kN-m)	Amp diff. (kN-m)
CFD	1456.35	–	93.93	–	9477.05	–	1588.24	–
Damping	1412.03	−3.04	83.60	−10.33	9759.49	2.98	1354.90	−233.34
Morison	1412.64	−3.00	113.21	19.28	9791.04	3.31	1841.58	253.34
Hybrid	1412.29	−3.03	114.70	20.77	9785.87	3.26	1869.99	281.75

Table 9
FOWT mooring tension mean value and oscillation amplitude comparison in rated wind and regular wave condition.

	M1				M2				M3			
	Mean val. (kN)	Mean diff. (%)	Amp. (kN)	Amp diff. (kN)	Mean val. (kN)	Mean diff. (%)	Amp. (kN)	Amp diff. (kN)	Mean val. (kN)	Mean diff. (%)	Amp. (kN)	Amp diff. (kN)
CFD	2988.12	–	128.25	–	1397.62	–	4.85	–	1382.85	–	5.21	–
Damping	2756.43	−7.75	81.31	−46.94	1411.82	1.02	6.35	1.50	1411.46	2.07	6.37	1.16
Morison	2776.27	−7.09	81.73	−46.52	1412.24	1.05	5.47	0.62	1408.78	1.88	5.49	0.28
Hybrid	2781.71	−6.91	80.81	−47.44	1411.95	1.03	5.55	0.70	1408.51	1.86	5.60	0.39

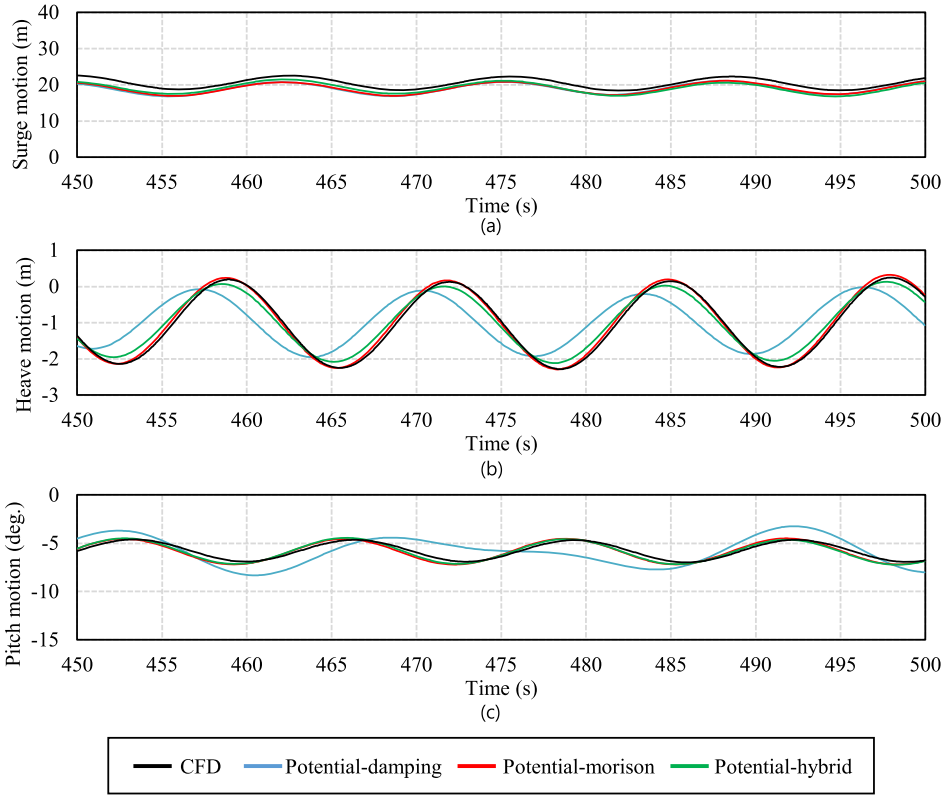

Fig. 22. FOWT 3DoF response result with cut-out wind condition.

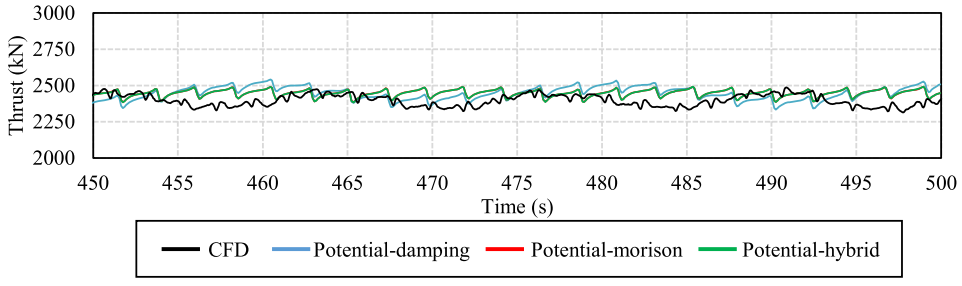

Fig. 23. FOWT aerodynamic performance result with cut-out wind condition.

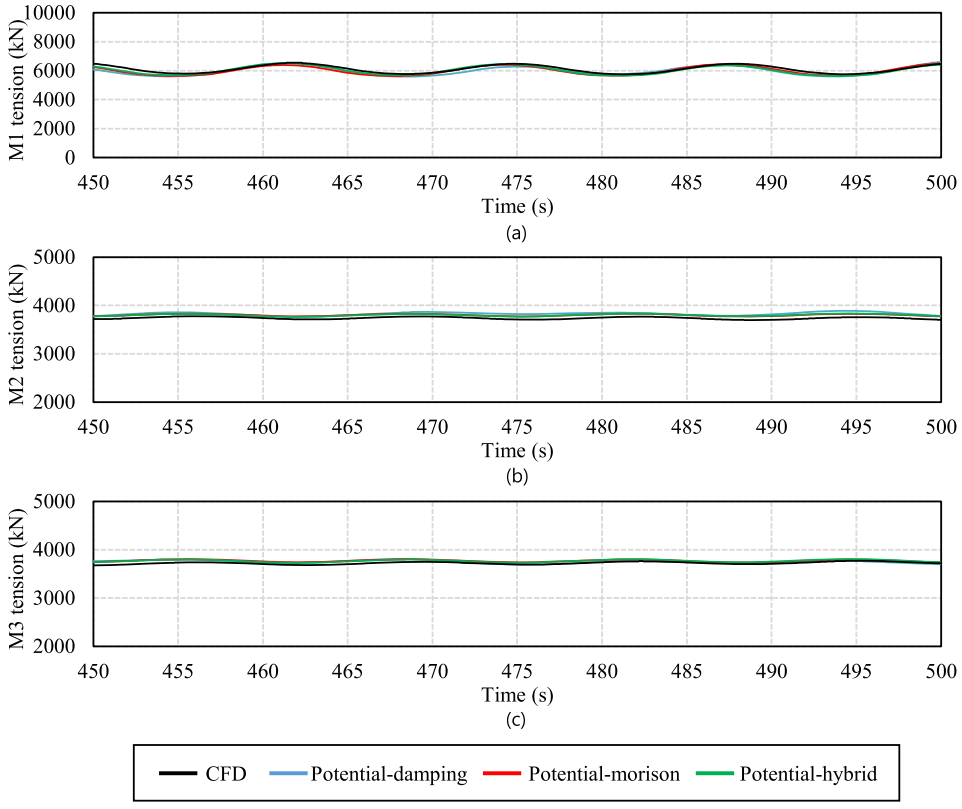

Fig. 24. FOWT mooring tension result with cut-out wind condition.

Table 10
FOWT 3DoF mean drift and oscillation amplitude comparison in cut-out wind condition.

	Surge				Heave				Pitch			
	Mean drift (m)	Mean diff. (%)	Amp. (m)	Amp diff. (m)	Mean drift (m)	Mean diff. (%)	Amp. (m)	Amp diff. (m)	Mean drift (deg.)	Mean diff. (%)	Amp. (deg.)	Amp diff. (deg.)
CFD	20.50	–	1.94	–	−0.90	–	1.20	–	−5.77	–	1.13	–
Damping	18.95	−7.56	1.89	−0.05	−0.86	−4.44	0.89	−0.31	−5.86	1.56	1.36	0.23
Morison	19.10	−6.83	1.90	−0.04	−0.87	−3.33	1.23	−0.03	−5.86	1.56	1.32	0.19
Hybrid	19.08	−6.93	1.96	0.02	−0.87	−3.33	1.05	−0.15	−5.85	1.39	1.31	0.18

Table 11
FOWT aerodynamic performance average value and oscillation amplitude comparison in cut-out wind condition.

	Thrust			
	Average (kN)	Avg diff. (%)	Amp. (kN)	Amp diff. (kN)
CFD	2397.46	–	88.00	–
Damping	2445.57	2.01	104.87	16.87
Morison	2447.48	2.09	54.43	−33.57
Hybrid	2447.27	2.08	54.77	−33.23

and oscillation amplitudes of 3DoF motion for the FOWT under cut-out wind conditions. For surge motion, the predicted mean drift exhibited a deviation of approximately 7 % across all correction methods, while the oscillation amplitudes closely matched CFD results, with differences limited to 0.05 m. In the case of heave motion, the mean values demonstrated strong agreement within a 5 % margin for all methods; however, notable discrepancies were observed in oscillation amplitudes when using the Damping method. For pitch response, mean values showed less than 2 % variation across all methods, with oscillation amplitudes differing by no more than 0.2° compared to CFD results.

Fig. 23 presents the time-series thrust response of the FOWT under

Table 12
FOWT mooring tension mean value and oscillation amplitude comparison in cut-out wind condition.

	M1				M2				M3			
	Mean val. (kN)	Mean diff. (%)	Amp. (kN)	Amp diff. (kN)	Mean val. (kN)	Mean diff. (%)	Amp. (kN)	Amp diff. (kN)	Mean val. (kN)	Mean diff. (%)	Amp. (kN)	Amp diff. (kN)
CFD	6131.41	–	379.76	–	3746.89	–	29.36	–	3714.66	–	32.36	–
Damping	6007.70	−2.02	364.91	−14.85	3803.25	1.50	35.96	6.6	3772.51	1.56	35.58	3.32
Morison	6032.80	−1.61	392.03	12.27	3800.55	1.43	28.83	−0.53	3769.73	1.48	29.29	−3.07
Hybrid	6031.49	−1.63	390.42	10.66	3800.81	1.44	30.48	1.12	3769.86	1.49	30.94	−1.42

cut-out wind conditions, comparing CFD simulations with three correction methods. Despite high wind speeds and a 0-degree pitch angle, all PBDC methods demonstrated thrust predictions closely matching the CFD results, with a deviation of approximately 2 % across all correction methods. Typically, aerodynamic force fluctuations are affected by surge and pitch motion, and the phase combination of these responses can suppress thrust oscillation amplitudes, preventing the development of distinct periodicity. The PBDC results did not show clear periodic variations except for the tower shadow effect. Meanwhile, in CFD simulations, slight periodic fluctuations were observed due to phase differences in surge motion compared to PBDC methods, though the oscillation amplitudes remained small. Additionally, the turbine used in this study requires blade pitch adjustment at a wind speed of 24 m/s, but the investigation was conducted without modifying the pitch angle to evaluate the consistency of PBDC predictions against CFD results. The findings indicate that CFD exhibited unstable thrust variations under unregulated blade conditions, whereas PBDC produced smoother thrust variations. This difference is attributed to CFD's higher sensitivity in capturing stall effects under these conditions.

Fig. 24 presents the mooring line tension of the FOWT under cut-out wind conditions, emphasizing the influence of increased mooring line weight on load responses. For mooring line M1, which experienced the highest loads, the average tension increased relative to prior analyses due to the added weight. However, the reduced surge mean response associated with the increased weight resulted in oscillation amplitudes that demonstrated improved alignment with CFD simulations. This behavior was consistent across all correction methods. Similarly, for mooring lines M2 and M3, the increased mooring line weight led to higher loads at the fairleads compared to previous analyses. Nevertheless, the load response patterns for these lines showed excellent agreement with CFD predictions across all correction methods.

Table 12 presents the numerical comparison of the tension results, where the average values for M1, M2, and M3 showed deviations of less than 2 % across all correction methods compared to CFD. This indicates a high level of accuracy in predicting mooring line tensions under extreme environmental conditions.

6. Conclusion

This study investigates the load response of a 10 MW FOWT using three approaches: damping coefficient calibration, drag coefficient calibration, and a hybrid method. The predictive accuracy of each method was evaluated against CFD simulation results. The hybrid and Morison methods demonstrated high accuracy, maintaining consistent performance under real-world conditions. In contrast, the PBDC corrected solely with damping coefficients exhibited inaccuracies in load response under varying environmental conditions, indicating limitations in its applicability. Free decay tests provided insights into platform dynamics but failed to fully capture complex environmental interactions involving waves, currents, and wind. To impose greater loads on the upper structure, the pitch angle was fixed, and load responses were assessed under extreme wind speeds. However, further studies are required to evaluate the efficacy of these correction methods when the turbine operates with a variable pitch angle, especially during extreme load scenarios. Notably, the study was conducted under regular wave conditions, whereas real-world environments are dominated by irregular wave patterns. Future research should explore the performance of the hybrid and Morison methods under irregular wave conditions to determine whether their accuracy is sustained.

In conclusion, the hybrid and Morison methods demonstrated high accuracy in predicting load responses under real-world conditions, enhancing the reliability of load estimation for FOWTs. Validation under both regular wave and extreme load scenarios confirmed the efficacy of these methods across diverse conditions. Nevertheless, the scope of this study was constrained to specific load scenarios, necessitating further investigation across a broader spectrum of environmental conditions. Since this study conducted analyses under only two environmental conditions, it has a limitation in terms of applicability. Therefore, future research will focus on conducting additional analyses across a broader range of wave conditions, including various wave heights and periods, to further strengthen the reliability of the proposed methodology. Furthermore, we plan to develop the hybrid method derived in this study by exploring and refining various hybrid correction approaches. This will enhance the accuracy and robustness of hydrodynamic modeling for floating offshore wind turbines.

CRediT authorship contribution statement

Ho-Seong Yang: Writing – review & editing, Writing – original draft, Visualization, Validation, Software, Methodology, Investigation, Formal analysis, Data curation, Conceptualization. **Ali Alkhabbaz:** Writing – review & editing, Software, Methodology. **Young-Ho Lee:** Writing – review & editing, Supervision, Project administration, Funding acquisition.

Declaration of competing interest

The authors declare that they have no known competing financial interests or personal relationships that could have appeared to influence the work reported in this paper.

Acknowledgements

This research was supported by Korea Institute of Energy Technology Evaluation and Planning (KETEP) grant funded by the Korean government (MOTIE) (20213000000030)—Development of disconnectable mooring system for A MW class floating offshore wind turbine.

References

Alkhabbaz, A., Hamza, H., Daabo, A.M., Yang, H.-S., Yoon, M., Koprulu, A., et al., 2024. The aero-hydrodynamic interference impact on the NREL 5-MW floating wind turbine experiencing surge motion. Ocean Eng. 295, 116970. https://doi.org/10.1016/j.oceaneng.2024.116970.

Bak, C., Zahle, F., Bitsche, R., Kim, T., Yde, A., Henriksen, L.C., et al., 2013. Description of the DTU 10 MW Reference Wind Turbine (Report No. I-0092). Department of wind energy. https://www.studocu.com/da/document/danmarks-tekniske-universitet/engelsk-1-us-civics-and-academic-writing-1/dtu-wind-energy-report-i-0092/46768724.

Böhm, M., Robertson, A., Hübler, C., Rolfes, R., Schaumann, P., 2020. Optimization-based calibration of hydrodynamic drag coefficients for a semisubmersible platform using experimental data of an irregular sea state. J. Phys. : Conf. Ser. 1669. https://doi.org/10.1088/1742-6596/1669/1/012023.

Clément, C., Bozonnet, P., Vinay, G., Pagnier, P., Nadal, A.B., Réveillon, J., 2022. Evaluation of Morison approach with CFD modelling on a surface-piercing cylinder towards the investigation of FOWT Hydrodynamics. Ocean Eng. 251. https://doi.org/10.1016/j.oceaneng.2022.111042.

Daabo, A.M., Alkhabbaz, A., Ibrahim, S.S., Hamzah, H., Hassan, A., Basem, A., Easa, H., Pavlovic, S., 2024. Thirteen vital factors for micro-scale radial turbine vane's design of geo-solar-powered Brayton cycle applications. Energy Convers. Manag. 315, 118774. https://doi.org/10.1016/j.enconman.2024.118774.

Edirisinghe, D.S., Yang, H.-S., Gunawardane, S.D.G.S.P., Alkhabbaz, A., Tongphong, W., Yoon, M., et al., 2023. Numerical and experimental investigation on water vortex power plant to recover the energy from industrial wastewater. Renew. Energy 204, 617–634. https://doi.org/10.1016/j.renene.2023.01.007.

Eurostat, 2019. 30% of electricity generated from renewable sources. https://ec.europa.eu/eurostat/web/products-eurostat-news/-/DDN-20180921-1.

Jonkman, J., Butterfield, S., Musial, W., Scott, G., 2009. Definition of a 5MW reference wind turbine for Offshore system development, NREL, TP-500-38060. https://www.nrel.gov/docs/fy09osti/38060.pdf.

Kvittem, M.I., Berthelsen, A., Eliassen, L., Thys, M., 2018. Calibration of hydrodynamic coefficients for a semi-submersible 10 MW wind turbine. ASME 2018 37th International Conference on Ocean, Offshore and Arctic Engineering 10 (10). https://doi.org/10.1115/omae2018-77826.

Lemmer né Sandner, F., Yu, W., Cheng, P.W., Pegalajar-Jurado, A., Borg, M., Mikkelsen, R.F., et al., 2018. The TripleSpar campaign: validation of a reduced-order simulation model for floating wind turbines, 10. ASME 2018 37th International Conference on Ocean. Offshore and Arctic Engineering. https://doi.org/10.1115/OMAE2018-78119.

Musial, W., Spitsen, P., Duffy, P., Beiter, P., Shields, M., Hernando, D.M., Hammond, R., Marquis, M., King, J., Sriharan, S., 2023. Offshore wind market report: 2023 edition United States. https://doi.org/10.2172/1997466.

Palm, J., Eskilsson, C., Paredes, G.M., Bergdahl, L., 2016. Coupled mooring analysis for floating wave energy converters using CFD: formulation and validation. International Journal of Marine Energy 16, 83. https://doi.org/10.1016/j.ijome.2016.05.003.

Pegalajar-Jurado, A., Madsen, F.J., Bredmose, H., 2025. damping identification of the tetraspar floater in two configurations with operational modal analysis.

Petter, A., Berthelsen, Bachynski, E.E., Karimirad, M., Thys, M., 2016. Real-Time Hybrid Model tests of a braceless semi-submersible wind turbine: Part III calibration of a numerical model. ASME 2016 35th International Conference on Ocean, Offshore and Arctic Engineering 6. https://doi.org/10.1115/OMAE2016-54640.

Robertson, A., Jonkman, J., Vorpahl, F., Popko, W., Qvist, J., Frøyd, L., et al., 2014a. Offshore code comparison collaboration continuation within IEA wind task 30: phase II results regarding a floating semisubmersible wind system (Report No. CP-5000-61154). In: Offshore and Arctic Engineering Conference. https://www.nrel.gov/docs/fy14osti/61154.pdf.

Robertson, A., Jonkman, J., Masciola, M., Song, H., Goupee, A., Coulling, A., Luan, C., 2014b. Definition of the semisubmersible floating system for phase II of OC4. https://www.nrel.gov/docs/fy14osti/60601.pdf.

Robertson, A.N., Wendt, F., Jonkman, J.M., Popko, W., Dagher, H., Gueydon, S., et al., 2017. OC5 project phase II: validation of global loads of the DeepCwind floating semisubmersible wind turbine. Energy Proc. 137, 38. https://doi.org/10.1016/j.egypro.2017.10.333.

Robertson, A., Wendt, F., Jonkman, J., Bachynski, E., Gueydon, S., Schünemann, P., 2018. Assessment of experimental uncertainty for a floating wind semisubmersible under hydrodynamic loading (Report No. CP-5000-70877). Proceedings of the ASME 2018 37th International Conference on Ocean Offshore Mechanics and Arctic Engineering. https://www.nrel.gov/docs/fy18osti/70877.pdf.

Robertson, A., Bachynski, E.E., Gueydon, S., Wendt, F., Schünemann, P., 2019. Total experimental uncertainty in hydrodynamic testing of a semisubmersible wind turbine, considering numerical propagation of systematic uncertainty. Ocean Eng. 195. https://doi.org/10.1016/j.oceaneng.2019.106605.

Robertson, A.N., Gueydon, S., Bachynski, E., Wang, L., Jonkman, J., Alarcón, D., et al., 2020. OC6 phase I: investigating the underprediction of low-frequency hydrodynamic loads and responses of a floating wind turbine. J. Phys. Conf. 1618 (3). https://doi.org/10.1088/1742-6596/1618/3/032033.

Srinivas, A., Robertson, B., Gadasi, J.B., Simpson, B.G., Lomónaco, P., Ilzarbe, J.M.B., 2023. Impact of limited degree of freedom drag coefficients on a floating offshore wind turbine simulation, 11(1), 139. J. Mar. Sci. Eng. https://doi.org/10.3390/jmse11010139.

Venugopal, V., Varyani, K.S., Westlake, P.C., 2008. Drag and inertia coefficients for horizontally submerged rectangular cylinders in waves and currents. Proc. IME M J. Eng. Marit. Environ. 223 (1), 121. https://doi.org/10.1243/14750902jeme124.

Wang, L., Robertson, A., Jonkman, J., Yu, Y., Koop, A., Borràs Nadal, A., Li, H., Bachynski-Polić, E., Pinguet, R., Shi, W., Zeng, X., Zhou, Y., Xiao, Q., Kumar, R., Sarlak, H., Ransley, E., Brown, S., Hann, M., Netzband, S., Wermbter, M., Méndez López, B., 2021. OC6 Phase Ib: validation of the CFD predictions of difference-frequency wave excitation on a FOWT semisubmersible. Ocean Eng. 241. https://doi.org/10.1016/j.oceaneng.2021.110026.

Wang, L., Robertson, A., Kim, J., Jang, H., Shen, Z., Koop, A., et al., 2022a. Validation of CFD simulations of the moored DeepCwind offshore wind semisubmersible in irregular waves. Ocean Eng. 260. https://doi.org/10.1016/j.oceaneng.2022.112028.

Wang, Y., Chen, H., Koop, A., Vaz, G., 2022b. Hydrodynamic response of a FOWT semi-submersible under regular waves using CFD: verification and validation. Ocean Eng. 258. https://doi.org/10.1016/j.oceaneng.2022.111742.

Wang, L., Robertson, A., Jonkman, J., Yu, Y., 2022c. OC6 phase I: improvements to the OpenFAST predictions of nonlinear, low-frequency responses of a floating offshore wind turbine platform. Renew. Energy 187, 282. https://doi.org/10.1016/j.renene.2022.01.053.

Wendt, F.F., Andersen, M.T., Robertson, A.N., Jonkman, J.M., 2016. Verification and validation of the new dynamic mooring modules available in FAST v8 (Report No. CP-5000-65822). 26th International Ocean and Polar Engineering Conference. https://www.nrel.gov/docs/fy16osti/65822.pdf.

Wendt, F., Robertson, A., Jonkman, J., 2017. FAST model calibration and validation of the OC5-DeepCwind floating offshore wind system against wave tank test data (report No. CP-5000-68080). ISOPE 2017 27th International Ocean and Polar Engineering Conference. https://www.nrel.gov/docs/fy17osti/68080.pdf.

Yang, H.-S., Tongphong, W., Ali, A., Lee, Y.-H., 2023. Comparison of different fidelity hydrodynamic-aerodynamic coupled simulation code on the 10 MW semi-submersible type floating offshore wind turbine. Ocean Eng. 281, 114736. https://doi.org/10.1016/j.oceaneng.2023.114736.

Yang, H.-S., Alkhabbaz, A., Tongphong, W., Lee, Y.-H., 2024a. Cross-comparison analysis of environmental load components in extreme conditions for pontoon-connected semi-submersible FOWT using CFD and potential-based tools. Ocean Eng. 304, 117248. https://doi.org/10.1016/j.oceaneng.2024.117248.

Yang, H., Alkhabbaz, A., Tongphong, W., Lee, Y., 2024b. Cross-comparison analysis of environmental load components in extreme conditions for pontoon-connected semi-submersible FOWT using CFD and potential-based tools. Ocean Eng. 304. https://doi.org/10.1016/j.oceaneng.2024.117248.

Zhang, Y., Xu, H., Law, Y., Santo, H., Magee, A., 2023. Hydrodynamic analysis and validation of the floating DeepCwind semi-submersible under 3-h irregular wave with the HOS and CFD coupling method. Ocean Eng. 287. https://doi.org/10.1016/j.oceaneng.2023.115701.

Zhou, Y., Xiao, Q., Peyrard, C., Pan, G., 2021. Assessing focused wave applicability on a coupled aero-hydro-mooring FOWT system using CFD approach. Ocean Eng. 240. https://doi.org/10.1016/j.oceaneng.2021.109987.

Zou, Q., Lu, Z., Shen, Y., 2023. Short-term prediction of hydrodynamic response of a novel semi-submersible FOWT platform under wind, current and wave loads. Ocean Eng. 278. https://doi.org/10.1016/j.oceaneng.2023.114471.